Journal of Non-Crystalline Solids 368 (2013) 1–16

Contents lists available at SciVerse ScienceDirect

Journal of Non-Crystalline Solids

journal homepage: www.elsevier.com/locate/jnoncrysol

Failure of multimode optical fibers nano-structured by near ablation threshold single-shot femtosecond laser procedure

B. Delobelle [a,b,1], D. Perreux [a,1], P. Delobelle [a,*]

[a] Department DMA, FEMTO-ST (UMR CNRS 6174) University of Franche-Comté, 24 rue de l'Epitaphe, 25000 Besançon, France
[b] Department DOPMD, FEMTO-ST (UMR CNRS 6174) University of Franche-Comté, 16 route de Gray, 25030 Besançon Cedex, France

ARTICLE INFO

Article history:
Received 5 November 2012
Received in revised form 22 January 2013
Available online 22 March 2013

Keywords:
Optical fiber;
Failure;
Femtosecond laser;
Nano-structuration;
Weibull's statistics

ABSTRACT

The present paper deals with the study of the failure probability of nano-structured optical fibers when submitted to uniaxial tensile loading. A nano-structuration procedure of optical fibers thanks to near ablation threshold single shot femtosecond laser has been proposed. The ablation threshold energy E_{p0} for silica fiber is such that: $NA^2E_{p0}=15.5$ nJ, where NA is the numerical aperture of the objective to focus the laser inside the fibers. The rupture strength of the impacted fibers can be controlled through the pulse energy E_p, the numerical aperture NA, the number N_ℓ of nano-craters depending on the step dz of the position of the fiber surface into the focal region, the interval dx between each crater and the number n_ℓ of flaw lines. An additive combination of two classical Weibull's laws allows a good representation of the failure probability of the impacted fibers. A phenomenological model for the evolutions of the Weibull's parameters (exponents and scaling stresses) has been proposed and the experimental tendencies of the failure probability curves are fairly well described by the set of the model's equations (Eq. (27)).

1. Introduction

The use of optical fiber for structural composite monitoring is closely related with smart structure concept which emerged in the early 1990s. Smart structures describe mechanical and civil engineering structures that integrate a sensing system. This sensing system may help to identify structural wear, damage or deterioration.

Due to their versatility, robustness and easiness of integration, optical fiber sensors have rapidly been recognized as an ideal sensing tool for smart structures [1–7]. Compared to conventional electrical sensors, the technology of the optical fiber sensors has the following advantages: immune to electromagnetic interference, chemically inert, long term reliability, weakly intrusive thanks to its small size, resistant to nuclear and ionizing radiation. Due to their small size and generally permanent integration in the structure, optical fiber sensors are considered to be non-destructive and minimally invasive testing tool. Moreover, the embedded sensors are protected by the composite material and can be installed during production, avoiding external installation. The mechanical properties of the current optical fibers are still quite known [8–15]. However, as shown by Semjonov et al. [16] on nano-indented fibers with diamond cube corner, if synthetic flaws are generated on the surface or in the core of the fibers, it is possible to control the rupture strength of these modified fibers. These flaws act as local stress concentrators under strain, resulting in a much lower tensile strength than that of the initial fiber. Thus, embedment of such modified fiber into a composite structure can be used as strain sensors, as an example to detect if the structure has locally undergoes a given strain. This kind of sensor acts as a strain safety-fuse. To generate nanometric flaws, femtosecond laser micromachining is a versatile material processing technology for fabricating a wide range of micro and nano-structures in transparent media [17,18]. Due to the extremely short light-matter interaction time with femtosecond pulses, the ablation process is quasi-deterministic allowing a high degree of precision and reproducibility [19–24]. Many different physical processes are involved in the ablation process [23,25–28]. The drilling of nano-holes in dielectric materials with sub-wavelength characteristic dimensions is possible thanks to the highly nonlinear nature of the important multi-photon ionization process with precisely defined ablation threshold [19,20,24]. In two previous papers [29,30] a detailed study of the morphology of nano-craters drilled in borosilicate glass by single-shot femtosecond laser ablation near the ablation threshold has been reported and different relationships for the evolutions of the depths and the various diameters have been proposed. Moreover, for the present application, this technology permits the surface (or the core) of the silica fiber to be nano-structured through the coating without significant damage of the protective layer which represents a considerable advantage.

Hence, the present paper deals with the study of the failure probability of nano-structured optical fibers with femtosecond laser procedure when submitted to uniaxial tensile loading.

* Corresponding author. Tel.: +33 3 81 66 60 13; fax: +33 3 81 66 67 00.
E-mail address: patrick.delobelle@univ-fcomte.fr (P. Delobelle).
[1] Now at MAHYTEC, 210 avenue de Verdun, 39100 Dole, France.

0022-3093/$ – see front matter © 2013 Elsevier B.V. All rights reserved.
http://dx.doi.org/10.1016/j.jnoncrysol.2013.02.008

2. Experiments

2.1. Optical fibers

Experiments, optical structuration and mechanical tests have been carried out on FURUKAWA (OFS) multimode optical fibers coated with polyimide coating. The manufacturer code, the core, the cladding and the coating diameters of tested fibers are TCG-MA100H, 100 μm, 110 μm and 140 μm, respectively. When this kind of fiber with polyimide coating is embedded into a composite structure a good strength transfer between the composite and the fiber has been observed [31], which is not the case for other fibers with acrylate or ETFE (ethylene tetrafluoroethylene) coatings. This is the main raison why this kind of fiber has been chosen to realize a mechanical sensor [31]. Note that the way the strength is transmitted to the fiber is not perfectly known.

2.2. Optical experimental setup

The amplified laser source (Spitfire ProV, Spectra-physics) emits 120 fs laser pulses with a central wavelength λ of 800 nm, at a repetition rate of $f = 5$ kHz. An independent Pockels cell system with a thin-film polarizer plays the role of an optical shutter that enables single-shot illuminations. A set of neutral densities allows adjusting the pulse energy. A polarizing cube and a zero-order quarter wave plate allow the production of a circular polarization before the laser beam passes through a microscope objective (MO), focusing onto the surface of optical fiber. Two types of Olympus Plan-fluor infinitely-corrected microscope objectives were used: ×20 with 0.4 numerical aperture (NA) and ×50 with 0.8 NA. As the beam diameter is far larger than the entrance aperture of the MO, the Airy spot sizes are 2.4 μm and 1.2 μm.

Thanks to a small device the optical fibers were mounted over a 3D positioning motorized stage (Newport ILS M-VP25) with bidirectional repeatability better than 200 nm and the sample orthogonality with respect to the beam propagation was ensured to be less than 1 mrad. The positioning of the fibers was achieved by imaging on a CCD camera with depths of field of 2 μm and 0.5 μm with the ×20 MO and ×50 MO, respectively.

Specific care has been devoted to the cleanliness of the beam. The dispersion of all optics was pre-compensated with the compressor of the chirped-pulse amplifier of the laser chain. The pre-compensation was carefully adjusted by measuring the pulse duration τ with a GRENOUILLE after the laser beam passed through the microscope objective and was collimated by a thin lens with negligible dispersion. The measured pulse duration is about $\tau = 120$ fs. The transmitted laser power P, just after the microscope objective, has been measured with a calibrated power-meter (GENTEC, XLP 12) whose measure range is $10\ \mu W < P < 3$ W corresponding to a pulse energy E_p in the range $2 nJ < E_p < 6\ 10^5$ nJ. Single-shot illuminations of the fiber were performed under atmospheric conditions for different pulse energies in the range of 16 nJ to 376 nJ, near the ablation threshold of silica.

2.3. SEM and AFM measurements

Some geometrical characterizations of the exact shape of nano-craters structured on the surface of optical fibers have been performed to evaluate the ablation threshold of the doped silica which constitutes the core and the cladding of the fibers. So, after metallization, selected nano-holes have been characterized by direct scanning electron microscopy imaging (SEM, Raith-Eline) and atomic force microscopy (AFM, PSIA XE-150).

2.4. Mechanical setup

To evaluate the distribution of probability of failure of optical fibers impacted by femtosecond laser shoot, tensile tests on relatively short specimens have been carried out. A DMA (Dynamic Mechanical Analysis) Bose Electroforce 3200 device with a cell load of 450 N has been used. The useful length of the specimens is fixed at 30 mm and the tests have been realized at 0.02 mm/s and room temperature. At least 20 to 30 specimen testing were required to be able to evaluate the distribution of probability of failure. However, gripping the fiber is the major problem and presently the samples have been glued and tightened between two card tabs to obtain a sufficient friction with the fiber to avoid slipping.

Moreover, for these short specimens, the load train and fiber must be accurately aligned in order to avoid preferential failure caused by bending between fiber and grips. With this procedure about 90% of the failures occur in the beam impacted zone i.e. in the middle of the useful length. During tensile tests, the cross head displacement has been measured with a Mach–Zendher optical interferometer. The force-displacement curves are perfectly linear, no slide has been observed and the failure suddenly happens. This is a characteristic of brittle materials. For virgin fibers the stress–strain curve slop is consistent with a 73 ± 8 GPa Young's modulus in accordance with the known theoretical value of silica. The fiber elongation is about 7.5%.

3. Preliminary results: ablation threshold of silica fiber

In two previous papers [29,30] a detailed study of the morphology of nano-craters drilled in borosilicate glass (Erie Scientific Micro Cover Glasses, Square1) by single shot femtosecond laser near the ablation threshold has been reported. The influence of numerical aperture (NA = 0.4 and 0.8), the pulse energy E_p and the position of the specimen surface into the focal region were thoroughly investigated. As a function of these parameters two kinds of nano-hole morphologies were reported. As shown in Fig. 1a,b the nano-holes were composed of a single crater (example Fig. 1a) or of two characteristic craters with very distinct geometries (example Fig. 1b). The two craters are quasi axi-symmetric along the laser beam axis and surrounded by a hemi-torus rim. Fig. 1c gives the scheme of a typical profile as well as the characteristic dimensions (widths and depths) for the main crater (index 1) and the second crater (index 2). The first crater is due to the incoming Gaussian pulse and the second to a spontaneous reshaping of the beam which transforms the incoming beam into a Gaussian–Bessel pulse [30]. As a function of the pulse energy E_p, the ablation threshold E_{p0}, the NA and the z position of the waist of the beam, different relationships were proposed for the evolution of the depths (h_1, h_2) and the diameters (L_1, L_2).

However, as previously mentioned, the experimental analysis and the different relations have been established on borosilicate glass, which is quite different of the silica fiber. Hence, to check the validity of these relations and particularly to determine the exact value of the ablation threshold, some experiments have directly been carried out on the fiber material. To do that, some fibers have been cleaved and the same experimental procedure than the one used for borosilicate glass, has been performed on the cross section of the fibers. Note that these experiments are difficult to properly realize. Hence, for each power, the sample was translated through the focal region, in the vertical direction Z, by steps of 250 nm over a range of 15 μm. After each laser shot corresponding to a fixed z value, the fiber was translated in plane by 5 μm in the X direction. After eight shoots on the same line in the X direction, a new line of eight shoots was realized with the same origin of the first one, but translated of 15 μm in the Y direction. Then this sequence has been repeated ten times, covering the Z focal region over 15 μm [29,30]. As shown in Fig. 2, for each studied power, this procedure allows a compact area of the silica fiber to be nano-structured. As a function of the pulse energy E_p and for NA = 0.4, the length ΔZ of the focal region where a visible laser-surface fiber interaction has been measured by optical or SEM imaging.

An example is given in Fig. 2. Indeed, ΔZ (μm) = 0.25 N where N is the number of observable impacts. In Fig. 3, for fiber glass as well as for

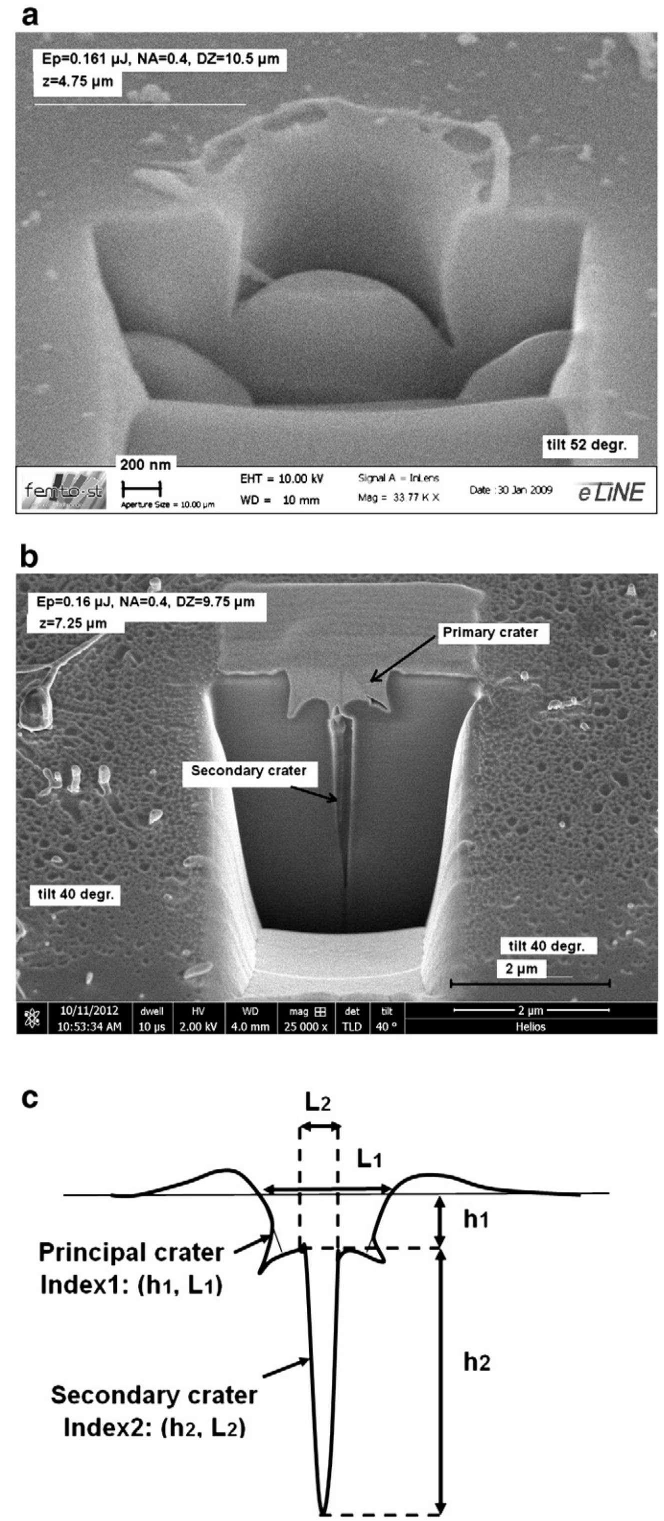

Fig. 1. a,b,c: SEM imaging of two different craters after FIB drilling. a) $E_p = 162$ nJ, NA = 0.4, z = 4.75 μm < ΔZ/2 = 5.25 μm. Only one crater is visible (primary crater). b) $E_p = 160$ nJ, NA = 0.4, z = 7.25 μm > ΔZ/2 = 4.87 μm. Two characteristic craters appear as z > ΔZ/2. c) Diagram of the crater morphology, definition of the different dimensions.

borosilicate glass for comparison [30], the length ΔZ has been plotted as a function of NA^2E_p. Note that, after the coating has been removed, some experiments have been performed along a generating line of the fiber. In that case the nano-structuration is linear and the very small inclination of the fiber together with the difficulty to exactly follow a generating line causes the ΔZ values to be slightly underestimated.

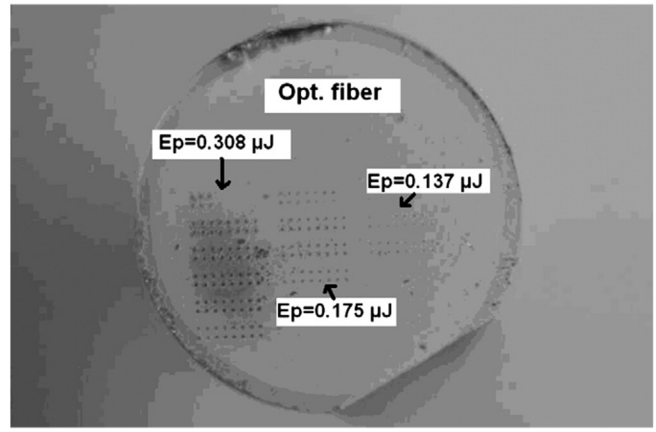

Fig. 2. Example of a global view of the laser shot path on a cross section of a cleaved fiber. ΔZ determination for $E_p = 0.137$, 0.175 and 0.308 μJ.

This is especially true for the large ΔZ. The ΔZ values for the fiber glass are clearly smaller than those measured in the borosilicate glass, thus the ablation threshold is greater. It has been shown [29,30] that:

$$\Delta Z = 2z_0\sqrt{\frac{F}{F_0}-1} = \frac{2\pi\alpha^2\lambda}{M^2NA^2}\sqrt{\frac{E_pNA^2}{\alpha^2\pi\lambda^2F_0}-1} \tag{1a}$$

as:

$$z_0 = \frac{\pi\omega_0^2}{\lambda M^2} \text{ and } \omega_0 = \frac{\alpha\lambda}{NA} \tag{1b}$$

z_0 is the Rayleigh range, ω_0 is the beam waist of the Gaussian beam, F and F_0 the fluence and the fluence threshold of the beam, λ the wavelength, M ~ 1 a parameter which characterizes the beam divergence and α a coefficient equal to 0.61 for a classical Airy disk. The relation (1) is recasted as:

$$\Delta Z = \frac{a_2}{NA^2}\sqrt{\frac{E_pNA^2}{a_1}-1} \quad \text{with } a_1 = \alpha^2\pi\lambda^2F_0 \quad \text{and} \quad a_2 = \frac{2\pi\alpha^2\lambda}{M^2}. \tag{2}$$

The two continuous curves in Fig. 3 correspond to $a_1 = NA^2E_{p0} = 11$ nJ and $a_2 = 1.21$ μm for borosilicate glass [30] and $a_1 = 15.5$ nJ and $a_2 = 1.21$ μm for silica fiber. With α = 0.491 and if M = 1 [30] then $F_0 = 2.3$ Jcm^{-2} for borosilicate which is consistent with the values reported in the literature [25,26,32], and $F_0 = 3.2$ Jcm^{-2} for silica fiber. As a first conclusion, only the ablation threshold value has to be changed in relations (1) and (2).

Now, as long as the dimensions of the primary craters are concerned, it has been shown in the literature and the two previous papers [29,30] that the maximum of the mean diameter value $<L_{1max}>$ [19,25,27,29,30] and $<h_{1max}>$ of the mean depth [29,30] are given by:

$$<L_{1\,max}> = 2\beta_L\ \omega_0\sqrt{Ln\left(\frac{F}{F_0}\right)} = \frac{2\beta_L\alpha\lambda}{NA}\sqrt{Ln\left(\frac{E_pNA^2}{a_1}\right)} \tag{3}$$

$$<h_{1\,max}> = \beta_h\ \omega_0 Ln\left(\frac{F}{F_0}\right) = \frac{\beta_h\alpha\lambda}{NA}Ln\left(\frac{E_pNA^2}{a_1}\right). \tag{4}$$

ω_0 is the beam waist radius in air, $a_1 = 11$ nJ, $\beta_L = 0.68$ and $\beta_h = 0.59$ [30]. These maxima are obtained for z = ΔZ/2, when the waist of the Gaussian beam is focused at the surface of the sample. These two dimensions have been measured on the impacts drilled on the cross section of the fiber and the results $<L_{1max}>$ ($<h_{1max}>$ not reported in this paper) in borosilicate and fiber glasses are reported

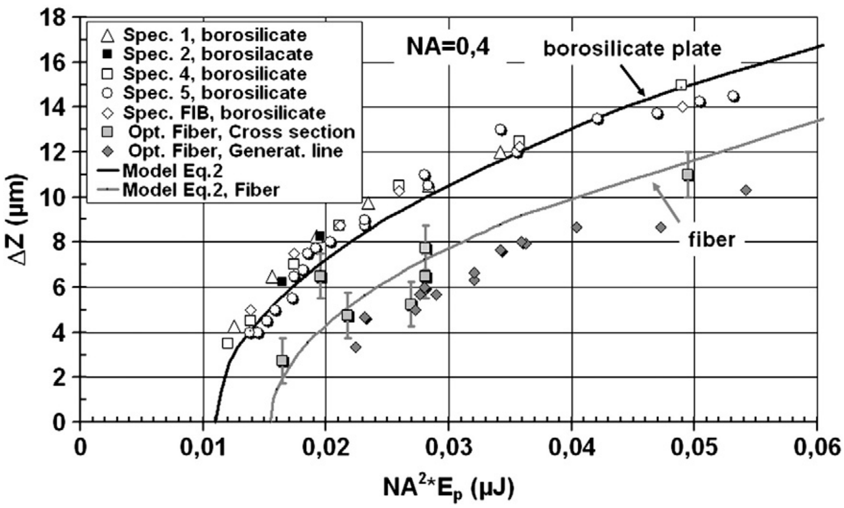

Fig. 3. Evolutions in borosilicate and optical fiber glasses of the length ΔZ of the focal region where the laser surface sample interaction is visible by direct imaging. Experiments and modeling.

in Fig. 4. As for ΔZ, the $<L_{1max}>$ and $<h_{1max}>$ values for the silica fiber are lower than those reported for the borosilicate. The two continuous curves drawn in Fig. 4 correspond to Eq. (3) with $a_1 = 11$ nJ and $a_1 = 15.5$ nJ for borosilicate glass and silica fiber, respectively. $2\beta_L\alpha\lambda = 535$ nm for the two materials. The same kind of result is obtained on $<h_{1max}>$, only the fluence threshold has to be changed in relations 2 to 4.

As a conclusion of these preliminary experiments the relations previously established on borosilicate glass for the ΔZ length and the dimensions of the primary craters remain valid for the silica fiber, only the ablation threshold energy has to be changed: $NA^2E_{p0} = 15.5$ nJ ($E_{p0} = 97$ nJ for NA = 0.4 and $E_{p0} = 24$ nJ for NA = 0.8). Due to experimental difficulties (focused ion beam sectioning of the holes in the cross section of the fiber), no measure has been performed on the secondary crater. However, we think that the previous conclusion drawn on the primary craters remains true for the secondary craters and thus [30]:

$$<L_{2\,max}> = \frac{\sqrt{2}\lambda}{\pi}\sqrt{1-\frac{F_{0c}}{F}} = \frac{\sqrt{2}\lambda}{\pi}\sqrt{1-\frac{a_3}{NA^2E_p}} \tag{5}$$

$$<h_{2\,max}> = \beta\frac{n_0}{n_0-1}z_0\sqrt{\mathrm{Ln}\left(\frac{F}{F_{0c}}\right)}\left(1+\sqrt{1-\frac{F_{0c}}{F}}\right) \text{ with } \frac{F}{F_{0c}} = \frac{NA^2E_p}{a_3} \text{ and } z_0 = \frac{\pi\omega_0^2}{M^2\lambda} \tag{6}$$

z_0 is the Rayleigh range, ω_0 the beam waist (Eq. (1b)), n_0 is the linear refractive index of the glass, $\beta \sim 0.24$ and $a_3 \sim 1.18\ a_1$. Note that the secondary craters appear at $z \sim \Delta Z/2$, when the waist of the beam is located inside the silica [30].

The previous mentioned conclusions have to be discussed, first from a material point of view and secondly from fiber geometry considerations. As previously shown the ablation threshold value is greater for silica fiber than for borosilicate glass. Indeed, the physical properties (thermal expansion, glass transition temperatures, refractive index…) slightly differ according to the exact chemical composition of the glass. Presently, the core of the studied fibers is composed of pure silica with high OH content (water content) and the clad of doped silica. From a physical point of view, due to the non linear nature of the interaction of femtosecond pulses with transparent materials, multi-photon absorption is required to initiate ablation. Hence, the optical breakdown threshold depends on the size of the band gap [17,20,23,24] and for a given material, on the material valence-

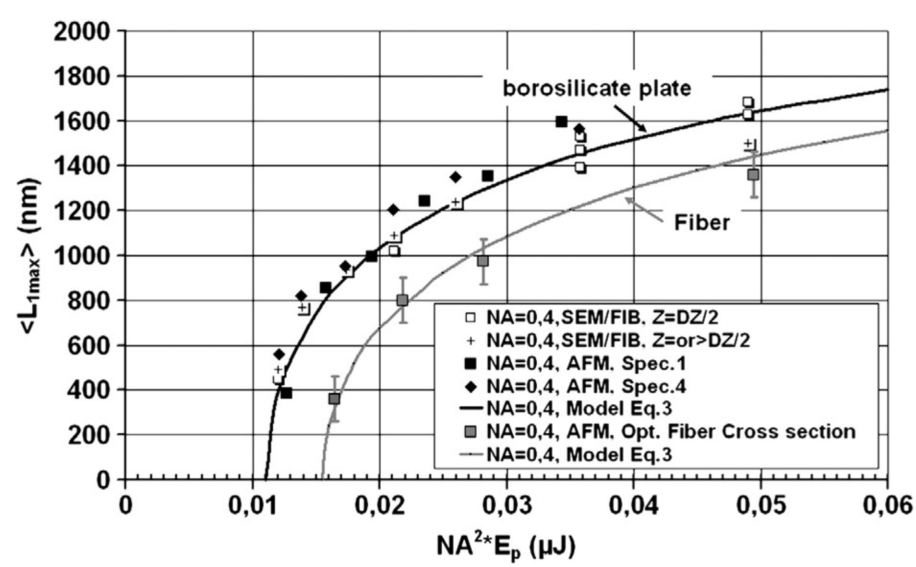

Fig. 4. Variation in borosilicate and optical fiber glasses of the upper diameter $<L_{1max}>$ as a function of NA^2E_p. Experiments and modeling.

electron spatial uniformity [22]. These two parameters are very sensitive to the chemical composition of the materials and this is the main reason of the variation of the threshold energy with the nature of the glasses (borosilicate or silica fibers). The presence of OH in the core of the fibers and doping elements in the clad is certainly responsible of the increase of the threshold. Note that for a good quality optical material the energy gap varies substantially over small scales but the valence-electron density, which is proportional to the atomic density is extremely uniform [22]. Moreover, for multi-mode fibers the refractive index in the clad n_{cl} is slightly lower than the one in the core and if n_{co} is the maximum value of the core index at its center the relative variation $\Delta n = n_{co} - n_{cl}/n_{co}$ is extremely small, in the order of 10^{-3}. Hence, the different parameters previously mentioned (Eqs. (1)–(6)) are quasi independent on Δn. From a theoretical point of view the waist beam is unaffected by the index variation, only the Rayleigh range z_0 varies as $\Delta z_0(\text{clad/core}) = \Delta n\ z_0(\text{core})$, thus the variation is negligible. In Fig. 3 it has been shown that the ΔZ values for the axial structured surfaces (generating line) are slightly lower than those for radial structuration (core of the fibers). It has been assumed that the inclination of the fiber and the difficulty to follow a generating line could explain this observation. A higher value of the clad threshold energy also could explain the lower ΔZ values. In that case, from the experimental points (along a generating line) in Fig. 3 a new threshold value can be determined: NA^2E_{p0} ~ 18.5 nJ, thus greater than the one in the core $NA^2E_{p0} = 15.5$ nJ. However, in Fig. 9 where the Weibull's scaling stresses have been plotted as a function of the pulse energy NA^2Ep, at least for $NA = 0.4$ and $NA^2E_P = 16.5$ nJ (in that case $\Delta Z = 2.9$ µm thus lower than the clad thickness $\Delta Z < 5$ µm) the scaling stresses are lower than those of virgin fibers. As a consequence, $NA^2E_{p0} < 16.5$ nJ. This is in accordance with $NA^2E_{p0} = 15.5$ nJ. Finally, we assumed that the nature of the axial and the radial structured surfaces is very close and that only the ablation threshold value has to be changed for the optical silica fibers.

4. Nano structuration of optical fibers

An experimental procedure has been developed to nano-structure the surface of the fibers through the coating without significant damage of the polyimide protective layer [31]. The scheme of this protocol is described on Fig. 5. As previously mentioned the coating thickness given by the manufacturer is equal to 15 ± 2.5 µm. Taking the refractive index of the polyimide, n_o ~ 1.7, into account, a translation of 9 µm in the air of the fiber along the vertical direction gives a displacement of 15 µm in the polyimide of the waist of the beam. Moreover, to include the different uncertainties on the geometric parameters of the fibers, their positions and the focusing on a generating line of the fiber (± 2 µm for $NA = 0.4$ and ± 0.25 µm for $NA = 0.8$), the imposed translation ΔZ_T is greater than the theoretical one (Eqs. (1): $\Delta Z_T = \Delta Z_{Theor.} \pm 5$ µm. To average the effects of the uncertainty on the position of the upper generating line, two or three lines (Fig. 5) of flaws are generated on the fibers. So, the sequence to nano-structure a fiber is given as follows: focusing on the upper generating line of the coating, translation of 9 µm in the Z direction to adjust the beam waist at the surface of the silica, new displacements in the Y and Z directions (Fig. 5) of dy and $\Delta Z_T/2$ µm, respectively. This position corresponds to the first laser impact. Then, a new displacement of dy in the Y direction allows to begin the second and then the third lines. After, the stage is translated of dx, −2dy, and dz (Fig. 5) to create the second impact of the first line. This sequence is repeated until the $\Delta Z_T/dz$ value. Thus, the experimental parameters of this nano-structuration are E_p, NA, dx, dy, dz and the number n_ℓ of lines. With this structuration, as previously mentioned and as shown in Fig. 6a–b, the brittle failure of the fiber is always initiated in the impacted zone by the laser beam.

5. Results and analysis of the mechanical tests

The most suitable and reliable law which allows describing the distribution of the probability P of failure of optical fibers is the Weibull's law [11,33–38]. Its common form is the two parameters Weibull distribution given by Eq. (7):

$$P(\sigma) = 1 - \exp\left(-L\left(\frac{\sigma}{\sigma_0}\right)\right)^{m_0} \tag{7}$$

where L is the length of the fiber, σ the applied tensile stress, σ_0 and m_0 the two scaling parameters: the Weibull's stress and the Weibull's modulus, respectively. A LnLn representation as expressed in Eq. (8) allows the determination of these two parameters, m_0 is the slope of the curve and σ_0 corresponds to the intersection with the stress axis.

$$\mathrm{Ln}\left[\frac{1}{L}\left(\mathrm{Ln}\frac{1}{1-P(\sigma)}\right)\right] = m_0[\mathrm{Ln}\ \sigma - \mathrm{Ln}\ \sigma_0]. \tag{8}$$

Assuming a group (i) of M samples, the cumulative failure probability $P(\sigma)$ for each of them is experimentally determined as follows:

$$P(\sigma_i) = \frac{i - 0.5}{M} \tag{9}$$

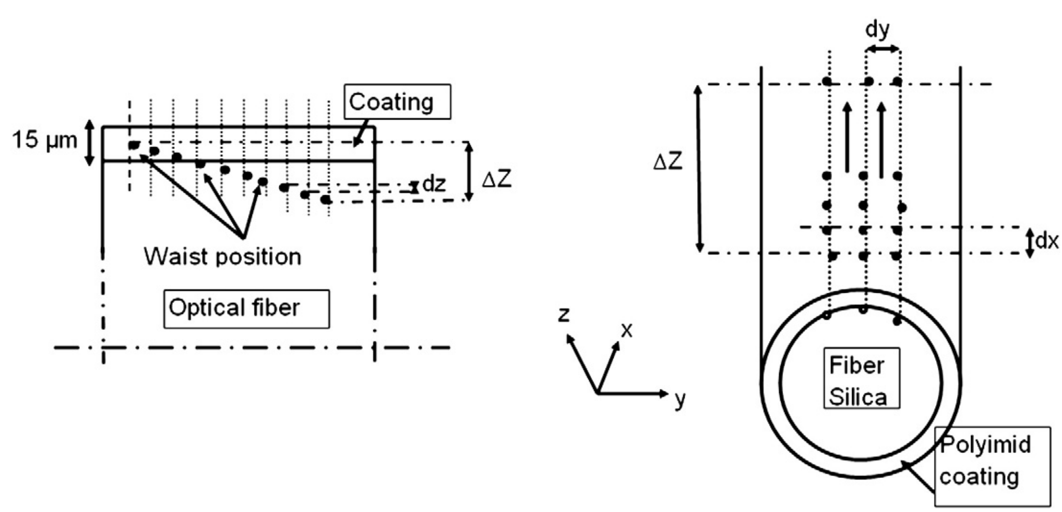

Fig. 5. Scheme of the nano-structuration procedure of optical fibers. Definition of dz, ΔZ, dy, and dx parameters.

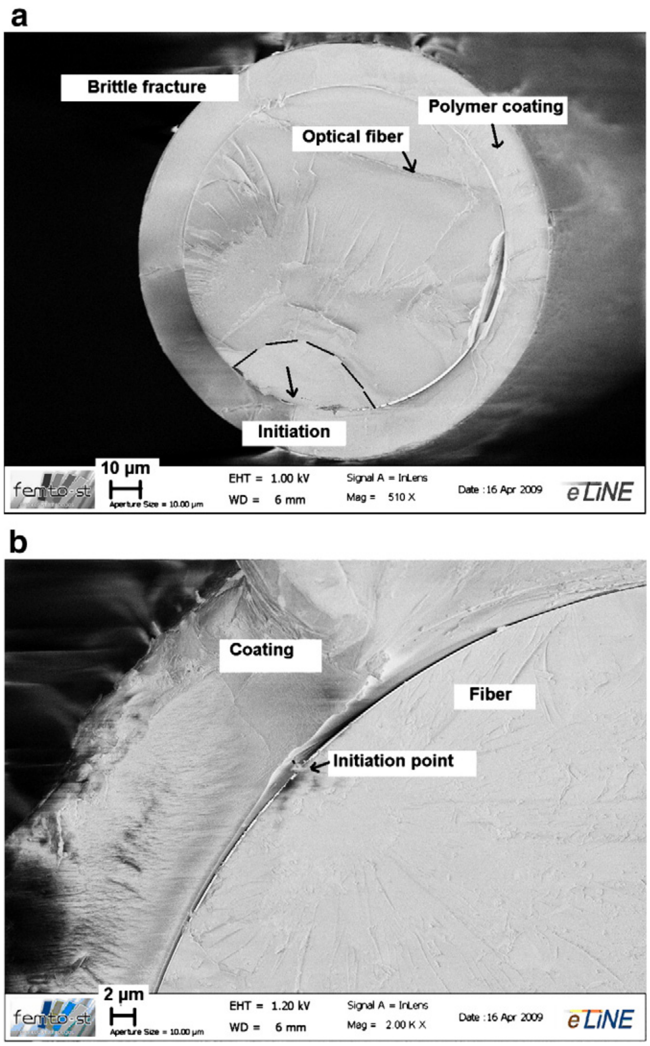

Fig. 6. a,b: a) Typical brittle fracture morphology of nano-structured optical fiber under tension. b) Zoom of the previous picture showing the location of the fracture origin.

and the failure stresses are listed in increasing magnitude as $\sigma_1 \le \sigma_2 \le \ldots \le \sigma_i \le \ldots \le \sigma_M$. A lot of experiments with NA = 0.4, dz = 0.33 μm and NA = 0.8, dz = 0.25 μm and different values of the pulse energy $E_{p0} = 97$ nJ < E_p < 376 nJ for NA = 0.4, $E_{p0} = 24$ nJ < E_p < 79 nJ for NA = 0.8, the geometrical parameters dx, dy, and n_ℓ being fixed, have been carried out. The results: probability of failure P as a function of the failure force is reported in Fig. 7a–b for NA = 0.4 and 0.8, respectively. The values of E_p, dx, dy, dz, n_ℓ and the number M (13 < M < 27) of retained experiments (rupture in the middle of the useful length of the fibers, ~90%) are specified in the figure captions. Moreover, some tests with fixed optical parameters (NA = 0.4 and E_p) but with different values of dx, dy and n_ℓ have also been performed and the results are reported in Fig. 7c. Of course, tests on non impacted fibers (E_p = 0 in the figures) have also been realized. From a qualitative point of view and as shown in Fig. 7(a,b,c), the probability of failure greatly depends on the optical parameters (NA, E_p) and in a less proportion on the structuration parameters (n_ℓ, dx, dy). Thus, P depends on the geometry and on the distribution of craters along the fibers. From a quantitative point of view, according to the Weibull's law (Eq. (8)), a $\mathrm{LnLn}(1/1-P)$ versus $\mathrm{Ln}\sigma$ representation of the results given in Fig. 7a,b,c has been done. An example is proposed in Fig. 8 for NA = 0.4 (data of Fig. 7a). Excepted for the non impacted fibers, the different curves are not linear but present a bilinear aspect. For virgin fibers the two Weibull's parameters, stress and exponent, are equal to $\sigma_{max} = 5310$ MPa and $m_{max} = 78$ which is in a fairly good agreement with the results given in the literature for short fibers (L < 0.8 m) [11,36–38], especially for the scaling stress ($4500 < \sigma_{max} < 5600$ MPa). This result a posteriori validates the method to grip and to test these short fibers. For laser beam impacted fibers the bilinear aspect of the Weibull's representation (Fig. 8) allows to determine four scaling parameters, σ_{01}, m_{01}, σ_{02}, and m_{02}, the index 01 being assigned to the highest stress values, $\sigma_{01} > \sigma_{02}$, and the exponents m_{0i} have been associated to the stresses σ_{0i}. For NA = 0.4 and 0.8 the geometrical parameters being fixed (Fig. 7a,b,c) the evolutions of σ_{0i} and m_{0i} as a function of the pulse energy NA^2E_p are reported in Fig. 9a–b, respectively. The two scaling stresses rapidly decrease with the pulse energy from $\sigma_{max} = 5310$ MPa to about 1000 MPa and then slowly decrease. The range of the m_{0i} exponents is such that $4 < m_{0i} < 28$. Moreover, as shown in Fig. 9b, two domains of m_{0i} values with the mean values of 8 and 24 could appreciably be highlighted. This point will be discussed further.

As it will be shown in the next paragraph (modeling), to fit with a four Weibull's scaling parameters the entire kinetic of the probability of failure reported in Fig. 7a,b,c, the relation (10) has been applied. In this relation S_0 is the cross section of the silica part of the fibers.

$$P = 1-\sum_{i=1}^{2}\alpha_i\ \exp-\left(\frac{\sigma}{\sigma_{0i}}\right)^{m_{0i}} = 1-\sum_{i=1}^{2}\alpha_i\ \exp-\left(\frac{F}{F_{0i}}\right)^{m_{0i}} \text{ with } \sigma_{0i} = \frac{F_{0i}}{S_0} \text{ and } \sum_{i=1}^{2}\alpha_i = 1. \quad (10)$$

Thus, there are five parameters, σ_{01}, m_{01}, σ_{02}, m_{02} previously identified and reported in Fig. 9a,b and $\alpha_2 = (1-\alpha_1)$. The values of α_2 have been identified on the different sets of experimental points reported in Fig. 7a–c. The continuous black lines in these figures correspond to the relation (10) identified with the values of α_2 reported in Fig. 9c. The α_2 (or α_1) coefficient is appreciably constant with a mean value of 0.45 ± 0.12.

To normalize the two coordinates of the curves of Fig. 9a,b with respect to the Weibull's parameters of the unstructured fibers, σ_{max}, m_{max}, and to the ablation threshold energy E_{p0}, the new coordinates of the representations in the Fig. 10a–b are σ_{0i}/σ_{max} as a function of E_p/E_{p0}. Thus, $0.18 < \frac{\sigma_{0i}}{\sigma_{max}} < 1$ and $0.05 < \frac{m_{0i}}{m_{max}} < 1$ for $1 < \frac{E_p}{E_{p0}} < 3.9$, with $\sigma_{max} = 5310$ MPa, $m_{max} = 78$ and $E_{p0} = 97$ nJ for NA = 0.4, $E_{p0} = 24$ nJ for NA = 0.8. The σ_{0i}/σ_{max} stress ratios follow parallel decreases contrary to the m_{0i}/m_{max} exponent ratios which present opposite evolutions: m_{01}/m_{max} decreases from 1 to 0.1 ($m_{01} \sim 8$) and m_{02}/m_{max} increases from 0.05 to 0.34 ($m_{02} \sim 26$) with the E_p/E_{p0} ratio.

6. Phenomenological modeling

As shown in Appendix A, considering two mechanisms (j = 1,2) of rupture and two families (i = 1,2) of flaws (defects with one or two craters) created during the femtosecond laser nano-structuration,

Fig. 7. a,b,c: Weibull's failure probabilities P of origin and nano-structured fibers. Experiments and modeling. The structuration parameters are:

a) NA = 0.4, $E_{p0} = 97$ nJ, dx = 5 μm, dy = 7 μm, dz = 0.33 μm, $n_\ell = 3$ and from the right to the left: (E_p = 0, M = 23), (E_p = 104 nJ, M = 13), (E_p = 125 nJ, M = 19), (E_p = 136 nJ, M = 24), (E_p = 146 nJ, M = 24), (E_p = 157 nJ, M = 24), (E_p = 206 nJ, M = 18), (E_p = 320 nJ, M = 27), (Ep = 376 nJ, M = 20).

b) NA = 0.8, E_{p0} = 24, 2 nJ, dx = 5 μm, dy = 7 μm, dz = 0.25 μm, $n_\ell = 3$ and from the right to the left: (E_p = 0, M = 23), (E_p = 82 nJ, M = 9, nano-voids), (E_p = 39 nJ, M = 18), (E_p = 65 nJ, M = 17), (E_p = 79 nJ, M = 23),

c) NA = 0.4, E_{p0} = 97 nJ, (E_p = 0, M = 23), (E_p = 123 nJ, dx = 5 μm, dy = 7 μm, dz = 0.33 μm, n_ℓ = 3, M = 19), (E_p = 123 nJ, dx = dy = 5 μm, dz = 0.25 μm, n_ℓ = 2, M = 12), (E_p = 157 nJ, dx = 12 μm, dy = 12 μm, dz = 0.33 μm, n_ℓ = 3, M = 18), (E_p = 157 nJ, dx = dy = 2 μm, dz = 0.33 μm, n_ℓ = 3, M = 18), (E_p = 157 nJ, dx = 5 μm, dy = 7 μm, dz = 0.33 μm, n_ℓ = 3, M = 24).

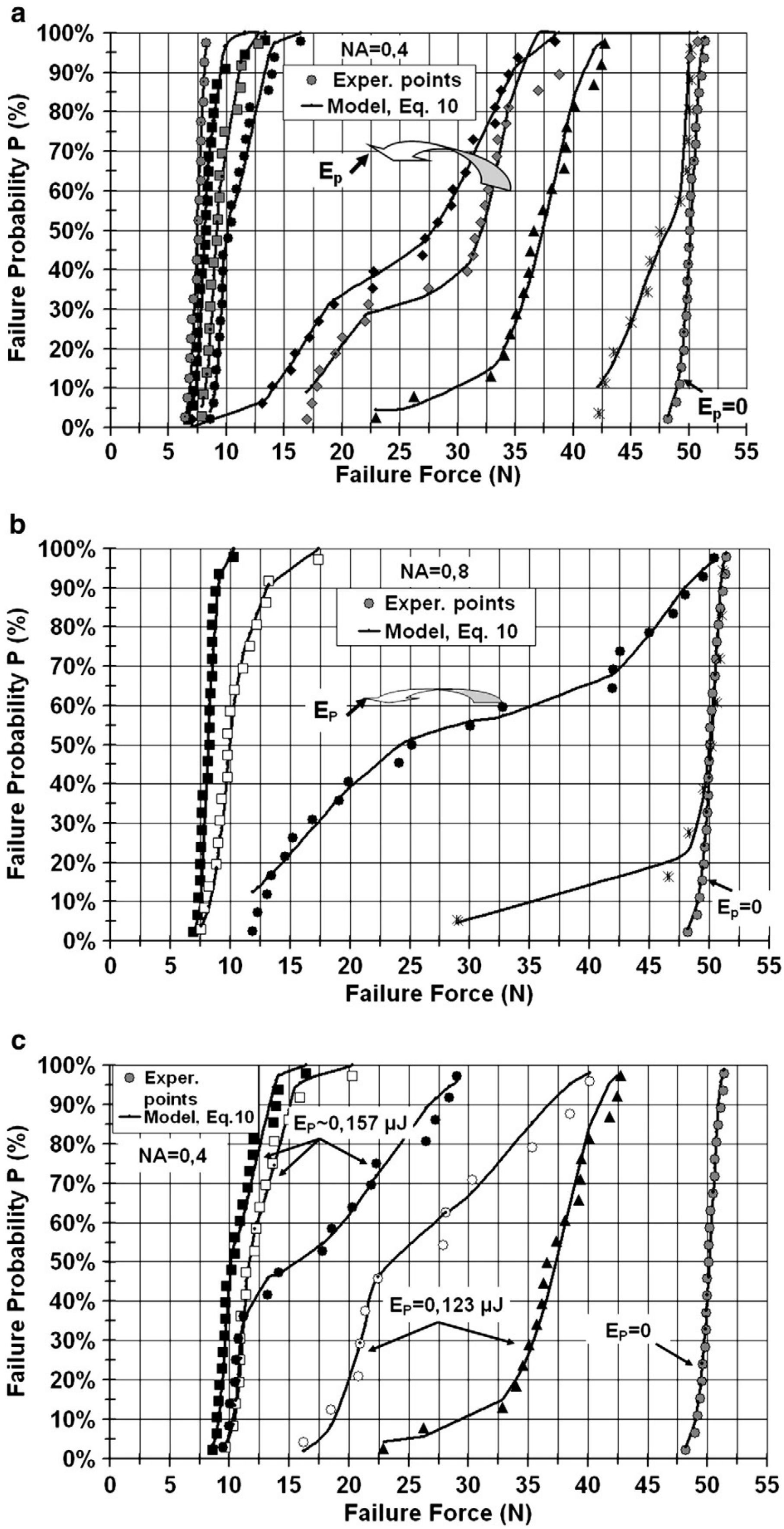
a
NA=0,4
Exper. points
Model, Eq. 10
E_p
E_p=0
Failure Probability P (%)
Failure Force (N)
b
NA=0,8
Exper. points
Model, Eq. 10
E_P
E_p=0
Failure Probability P (%)
Failure Force (N)
c
Exper. points
Model. Eq.10
NA=0,4
E_P~0,157 μJ
E_P=0,123 μJ
E_P=0
Failure Probability P (%)
Failure Force (N)

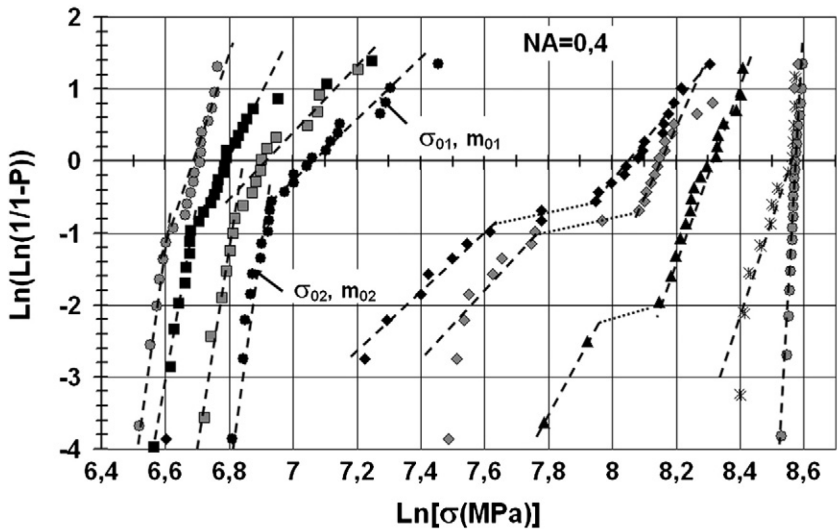

Fig. 8. Logarithmic representations (Fig. 7a) of the Weibull's law according to Eq. (8). Determination of the Weibull's parameters σ_{0i} and m_{0i}. Case of NA = 0.4: the identified laws (Eq. (10)) are reported in Fig. 7a.

the general form of the probability of failure P can be written as follows:

$$P = 1-\sum_{i=1}^{2}\alpha_i\ \exp-\left(\frac{\sigma_1}{\sigma_{0i}}\right)^{m_{0ii}} \text{with} \frac{\sigma_{0i}}{\sigma_{max}} = \sum_{i=1}^{2}\frac{\beta_j}{F_{ij}\left(\frac{\sigma_2}{\sigma_1},\frac{\sigma_3}{\sigma_1}\right)}$$
$$= \sum_{j=1}^{2}\frac{\beta_j}{1+f^*_{ij(nano-struct.)}} \text{ and } \frac{m_{0i}}{m_{max}} = g_i\left(\frac{\sigma_{0i}}{\sigma_{max}}\right),\ \sum_{i=1}^{2}\alpha_i = 1,\ \sum_{j=1}^{2}\beta_j = 1. \quad (11)$$

σ_1, σ_2, and σ_3 are the three principal stresses, β_j a coefficient, F_{ij}, f_{ij} and g_i are different functions depending on the stress tri-axiality, the nano-structuration parameters and the Weibull's stresses (σ_{0i}, σ_{max}), respectively. In the present case σ_1 is the tensile stress σ. A condensed form of the relation (11) is given by the Eq. (12):

$$P = 1-\sum_{i=1}^{2}\alpha_i \exp-\left(\frac{\sigma}{\sigma_{max}\sum_{j=1}^{2}\frac{\beta_j}{1+f^*_{ij(nano-struct.)}}}\right)^{m_{max}g_i\left(\frac{\sigma_{0i}}{\sigma_{max}}\right)}, \quad (12)$$
$$\sum_{i=1}^{2}\alpha_i = 1,\ \sum_{j=1}^{2}\beta_j = 1.$$

Note that for unstructured fibers, $f^*_{ij(nano\ \ struct.)} = 0$ and thus the Weibull's probability of failure is rewritten as (see Appendix A)

$$P = 1-\exp-\left(\frac{\sigma}{\sigma_{max}}\right)^{m_{max}}. \quad (13)$$

As shown in the Appendix A, the tri-axiality functions $F_{ij}\left(\frac{\sigma_2}{\sigma_1},\frac{\sigma_3}{\sigma_1}\right)$ are intimately linked to the geometry and the distribution of the craters. Two different scales have been considered depending on the dimensions of the craters and of the global structuration.

For the highest pulse energies ($NA^2E_p > 26$ nJ) during a tensile test, the generated stress field by the biggest crater is sufficiently large and the tri-axiality sufficiently high for the rupture initiates on the micro-cracks to lie inside the stress field of this defect. So, independently on the distribution of the craters, the rupture occurs in the vicinity of the biggest defect composed of one or two characteristic craters (Fig. 1a,b). Consequently, if the index j = 2 is associated to this scale, the functions f^*_{12} and f^*_{22} in Eqs. (11) and (12) must be identified. To evaluate these functions some finite element (FE) analysis has been realized with the Comsol software. A fiber with only one crater whose dimensions (h_1, L_1, h_2, L_2) are close to those experimentally determined and submitted to a tensile stress has been modeled. From the stress analysis the extension of the stress field around the primary crater is obtained much larger than the one around the secondary crater and thus the probability to initiate the failure on micro-cracks in the vicinity of the primary craters is fairly high. Moreover, as a function of the geometry of the crater the stress concentration factors, $K_{T2} = 1+\sigma_2/\sigma_1$ and $K_{T3} = 1+\sigma_3/\sigma_1$, have approximately been found as:

$$K_{T_i} = 1+k_i\sqrt{\frac{h_1}{L_1}} \text{ with } k_2 = 1.6 \text{ and } k_3 = 0.5. \quad (14)$$

Note that for a superficial elliptical flaw, Inglis [39] reports $K_{T_1} = 1+2\sqrt{\frac{h}{\rho}}$ where h is the flaw depth and ρ its tip radius. As a first approximation and as mentioned in the Appendix A, a mean value of the stress concentration factor K_{Teq} is given by:

$$K_{T_{eq}} \approx \frac{K_{T2}+K_{T3}}{2} = 1+\frac{k_2+k_3}{2}\sqrt{\frac{h_1}{L_1}} \text{ with } \frac{k_2+k_3}{2} = 1.05. \quad (15)$$

Combining the relations (3) and (4) the ratio h_1/L_1 can be determined:

$$\frac{h_1}{L_1} = \frac{\beta_h}{2\beta_L}\sqrt{\mathrm{Ln}\frac{E_p}{E_{p0}}} \text{ with } \beta_h/2\beta_L = 0.43, \quad (16)$$

and thus:

$$K_{T_{eq}} = 1+\gamma\left(\mathrm{Ln}\frac{E_p}{E_{p_0}}\right)^{1/4} \text{ with } \gamma = \frac{k_2+k_3}{2}\sqrt{\frac{\beta_h}{2\beta_L}} = 0.69. \quad (17)$$

As a consequence,

$$f^*_{12} = f^*_{22} = f^* = \gamma\left(\mathrm{Ln}\frac{E_p}{E_{p_0}}\right)^{r} \text{ with } \gamma = 0.69 \text{ and } r = 1/4. \quad (18)$$

Note that f^* is independent of the numerical aperture NA.

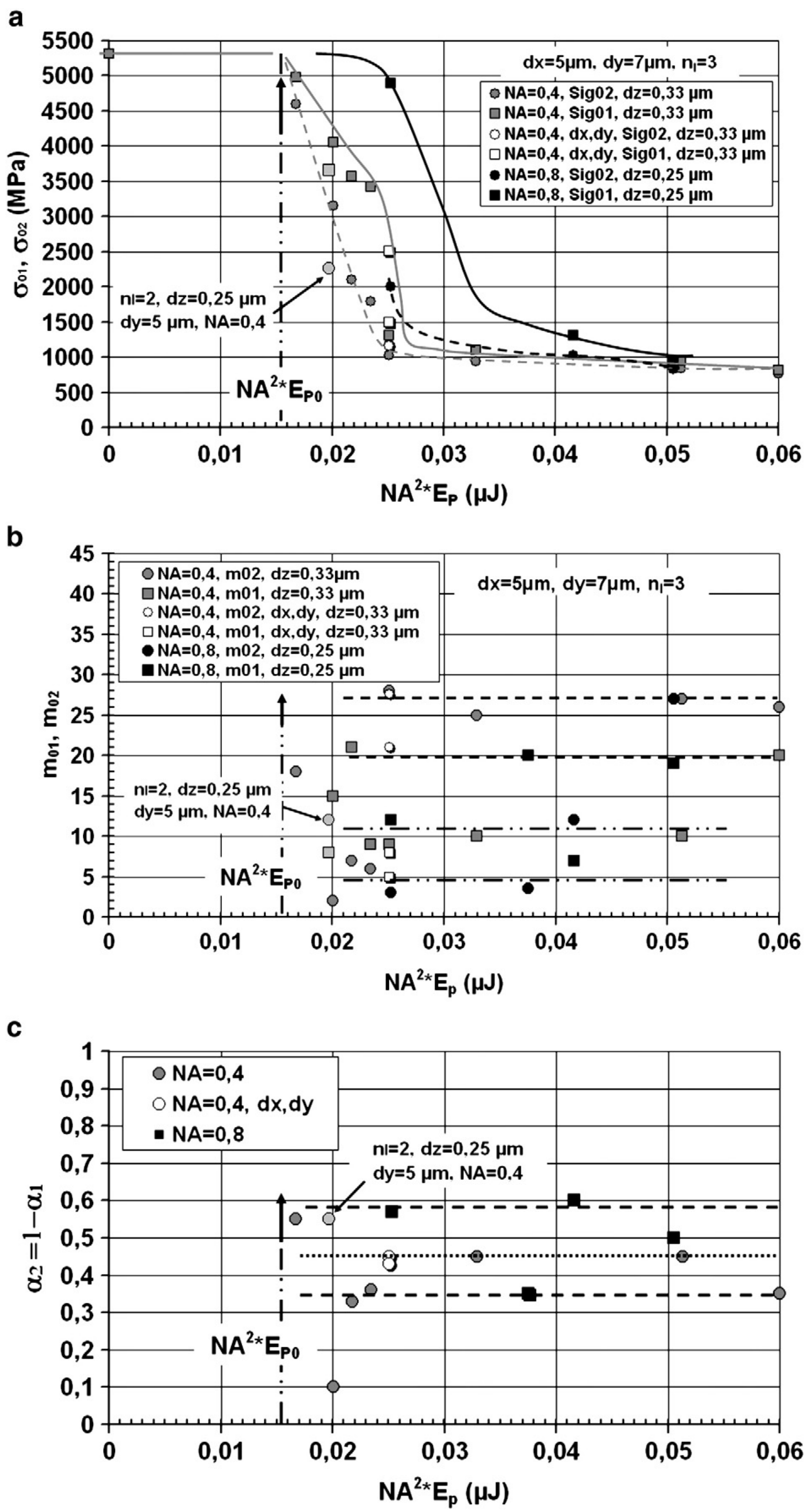

Fig. 9. a,b,c: Evolution of the five Weibull's parameters (Eq. (10)) for NA = 0.4 and 0.8 as a function of NA^2E_p. a) scaling stresses: σ_{01}, σ_{02}, b) exponents: m_{01}, m_{02}, c) ponderation parameter: $\alpha_2 = (1-\alpha_1) \sim 0.45 \pm 0.12$.

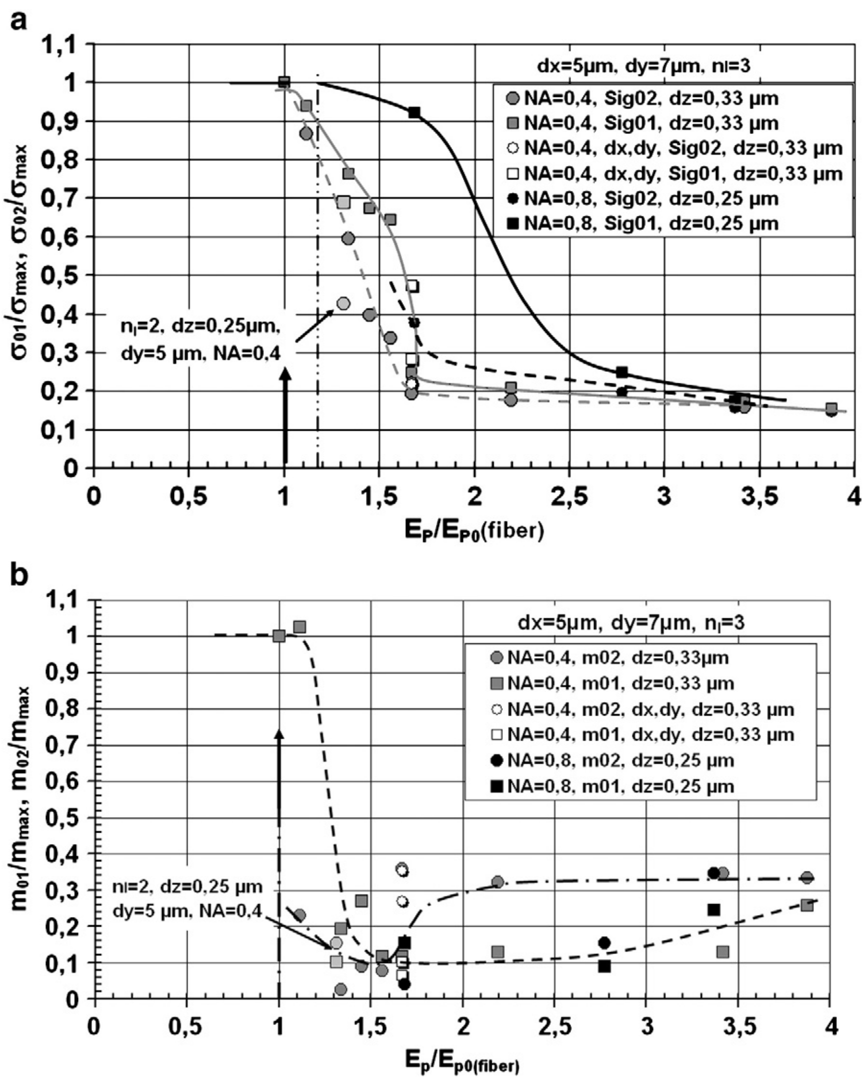

Fig. 10. a,b: Normalized Weibull's parameters with respect to those of unstructured fibers σ_{max}, and m_{max} as a function of the normalized energy E_p/E_{p0}. a) scaling stresses σ_{0i}/σ_{max}, b) exponents m_{0i}/m_{max}.

For the lower energies (NA^2E_p<26 nJ) the failure mechanism is complex. The dimensions of the defects are small, the two families of defects (1 or 2 craters) and the global structuration have been assumed to participate to the initiation of the rupture. Moreover, depending on the dy values, the stress fields generated by the craters of the different lines could interact. Thus, from a phenomenological point of view $f_{11}^* \neq f_{21}^*$. These two functions have been assumed to depend on the number $N_{\ell p}$ of defects with only one crater and $N_{\ell s} \approx N_{\ell p}$ of defects with two craters on one line, on the number n_ℓ of lines, on an interaction function $I(n_\ell, \mathrm{dy})$ between the stress fields of the different lines and, as previously shown (Eqs. (17) or (18)), on a function of the normalized energy $G(E_p/E_{p0})$. The general form is written as:

$$f_{i1}^* = N_{\ell_i} I(n_\ell, \mathrm{dy}) G_i\left(\frac{E_p}{E_{p_o}}\right). \tag{19}$$

Thanks to Eq. (1) the number N_ℓ of crater per line is easily shown equal to:

$$N_\ell = \frac{2z_0}{\mathrm{dz}}\sqrt{\frac{E_p}{E_{p0}}-1} = \frac{2\alpha^2\pi\lambda}{M^2NA^2\mathrm{dz}}\sqrt{\frac{E_p}{E_{p0}}-1} \text{ and } N_{\ell_p} \approx N_{\ell_s} \approx \frac{N_\ell}{2}. \tag{20}$$

Hence the f_{i1}^* functions vary as N_l thus as $1/NA^2dz$.

For $1<n_\ell<3$, $I(n_\ell, \mathrm{dy})$ has been defined as:

$$I(n_\ell, \mathrm{dy}) = \frac{2n_\ell}{1+\frac{3}{n_\ell} I_0\left(\frac{\mathrm{dy}}{\mathrm{dy}_0}\right)} \quad \text{with} \tag{21a}$$

$$I_o\left(\frac{\mathrm{dy}}{\mathrm{dy}_0}\right) = \begin{cases} 1+\left(\frac{\mathrm{dy}}{\mathrm{dy}_0}-1\right)H\left(\frac{\mathrm{dy}}{\mathrm{dy}_0}-1\right) & \text{for } 0<\mathrm{dy}<\mathrm{dy}_{max} \\ \frac{\mathrm{dy}_{max}}{\mathrm{dy}_0}+\left(\frac{\mathrm{dy}}{\mathrm{dy}_0}-\frac{\mathrm{dy}_{max}}{\mathrm{dy}_0}\right)H\left(\frac{\mathrm{dy}_{max}}{\mathrm{dy}_0}-\frac{\mathrm{dy}}{\mathrm{dy}_0}\right) & \text{for } \mathrm{dy}_0<\mathrm{dy}<R \end{cases}. \tag{21b}$$

H(.) is the Heaviside function ($H(x)=0$ if $x<0$ and $H(x)=1$ if $x\geq 0$), dy_0 is the minimum distance between two lines, of the order of $<L_{1max}>$ and which has been fixed at 2 µm. dy_{max} is the maximum distance between two lines above which (due to the circular cross section of the fiber) the nano-structuration due to the lateral lines is too weak and thus has no effect on the rupture of the fibers. dy_{max} has been fixed at 22 µm ~ R/2 (R is the radius of the fibers), then the height between the upper generating line and the lateral one is about R/8 ~ 7 µm. An application of Eqs. (21a) and (21b) for $n_\ell=3$ gives: $I = n_\ell = 3$ if $\mathrm{dy}<\mathrm{dy}_0$, $I=\frac{6}{1+\frac{\mathrm{dy}}{2}}$ if $\mathrm{dy}_0<\mathrm{dy}<\mathrm{dy}_{max}$ a decreasing function of dy, and $I=1/2$ if $\mathrm{dy}>\mathrm{dy}_{max}$. Note that $I=1/2$ corresponds to the case of $n_\ell=1$ ($\mathrm{dy}<\mathrm{dy}_0$) in Eqs. (21a) and (21b). For a large single isolated crater as previously shown G_i is a function of h_1/L_1 $\left(or\sqrt{Ln\,E_p/E_{p0}}(Eq.16)\right)$. However, for the overall structuration with small craters and as shown by Afferrante et al. [40] with numerical analysis at the crack level, the scaling stress σ_o greatly depends on the ratio between the ligament size d between micro-cracks and the mean value of the crack lengths a_{mean} (d/a_{mean}). From a theoretical point of view, as for the crack size (Eqs. (A4) or (A10)), a critical ligament size dc and a ligament size distribution have to be defined to evaluate the failure probability P [40]. So, F_{ij} in Eq. (11) depends on the stress tri-axiality and on the ligament size which is equally function of this tri-axiality, thus:

$$\mathrm{F}=\mathrm{F}\left(\frac{\sigma_2}{\sigma_1},\frac{\sigma_3}{\sigma_1},d^{-1}\left(\frac{\sigma_2}{\sigma_1},\frac{\sigma_3}{\sigma_1}\right)\right)\ \text{particularized as}\ \mathrm{F}=1+\frac{\mathrm{F_0}\left(\frac{\sigma_2}{\sigma_1},\frac{\sigma_3}{\sigma_1}\right)}{\mathrm{d}\left(\frac{\sigma_2}{\sigma_1},\frac{\sigma_3}{\sigma_1}\right)} \tag{22}$$

where d is a decreasing function of the stress tri-axiality and if d is proportional (for simplicity) to $\mathrm{F_0}\left(\frac{\sigma_2}{\sigma_1},\frac{\sigma_3}{\sigma_1}\right)^{-2q+1}$ then the relation (22) gives:

$$\mathrm{F}=1+\left(\mathrm{F_0}\left(\frac{\sigma_2}{\sigma_1},\frac{\sigma_3}{\sigma_1}\right)\right)^{2q}. \tag{23}$$

Combining the relations (11), (18), (20), (21a and 21b) and (23) the general equations for the evolution of the $\frac{\sigma_{0i}}{\sigma_{max}}$ ratio reads:

$$\frac{\sigma_{0i}}{\sigma_{\max}}=\frac{\beta}{1+\frac{2\delta_i n_\ell N_\ell}{1+\frac{3}{n_\ell}I_0\left(\frac{dy}{dy_0}\right)}\left(\mathrm{Ln}\left(\frac{\mathrm{E_p}}{\mathrm{E_{p0}}}\right)\right)^{q}}+\frac{1-\beta}{1+\gamma\left(\mathrm{Ln}\left(\frac{\mathrm{E_p}}{\mathrm{E_{p0}}}\right)\right)^{r}}. \tag{24}$$

$I_0\left(\frac{dy}{dy_0}\right)$ is given by Eq. (21b) and $N_\ell=\frac{2\alpha^2\pi\lambda}{\mathrm{M^2NA^2dz}}\sqrt{\frac{\mathrm{E_p}}{\mathrm{E_{p0}}}-1}$.

The four parameters β, δ_1, δ_2 and q have been adjusted on the experimental data and the σ_{0i}/σ_{max} ratio as a function of the number N_ℓ of craters over one line is reported in Fig. 11a. The cross symbols correspond to the exact experimental conditions and the different continuous (σ_{02}) or interrupted (σ_{01}) lines to the general evolutions given by the Eq. (24). There is a fairly good agreement with the experimental reality, even for $n_\ell=2$ and $dz=0.25$ µm.

Now, for the Weibull's exponents m_{0i}, as written in Eq. (11), $\frac{m_{0i}}{m_{max}}=g_i\left(\frac{\sigma_{0i}}{\sigma_{max}}\right)$. For all the experimental determinations (Fig. 7a–c), the $\frac{m_{0i}}{m_{max}}$ ratio (values given in Fig. 10b) as a function of the $\frac{\sigma_{0i}}{\sigma_{max}}$ ratios (values given in Fig. 10a) are reported in Fig. 11b. Of course, for $\frac{\sigma_{0i}}{\sigma_{max}}=1$, $\frac{m_{0i}}{m_{max}}=1$ and for $\frac{\sigma_{0i}}{\sigma_{max}}=0$, i.e. instantaneous rupture, it has been assumed that $\frac{m_{0i}}{m_{max}}=1$. Note that the exact values of m_{0i} for $\sigma_{0i}=0$ cannot be experimentally determined. Moreover, the $\frac{m_{0i}}{m_{max}}$ values present a

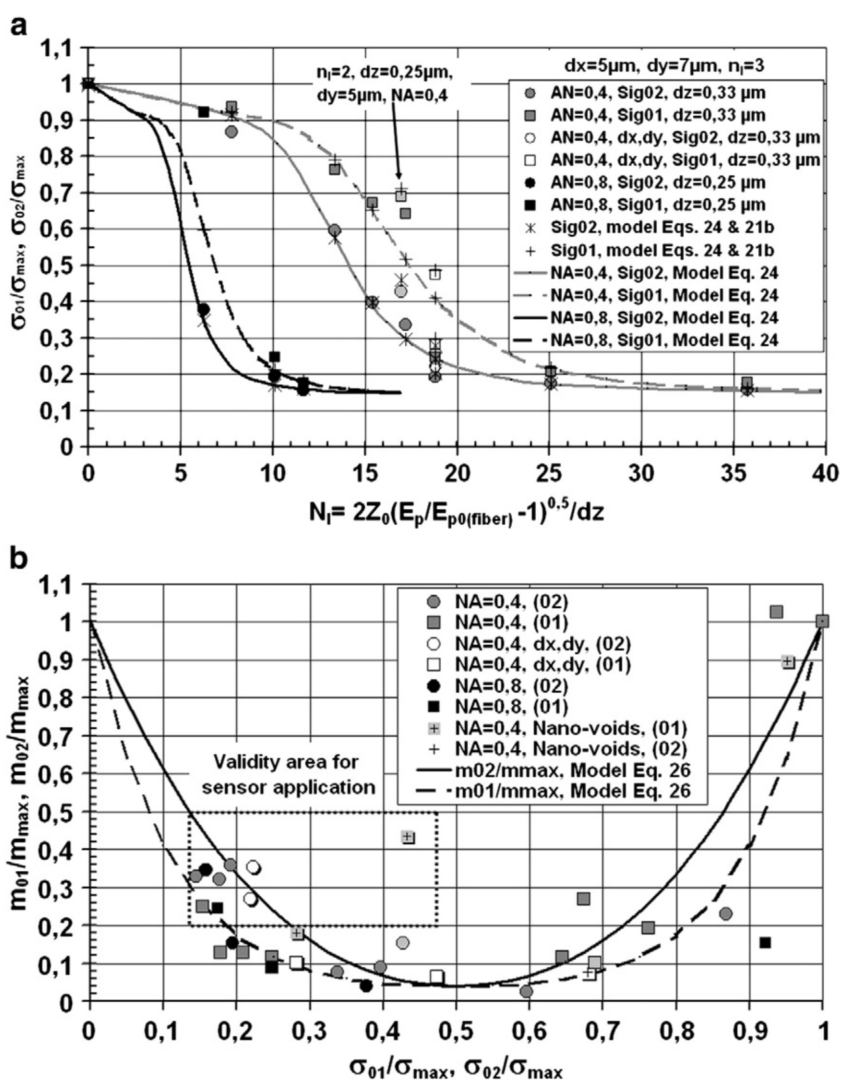

Fig. 11. a,b: Prediction of the Weibull's parameters values thanks to the complete model (Eq. (27)). a) σ_{0i}/σ_{max} as a function of the number of craters per line. The cross symbols correspond to the exact experimental conditions and the lines to the global evolutions (Eq. (24)). b) m_{0i}/m_{max} as a function of σ_{0i}/σ_{max}. The two lines correspond to Eq. (26) with $p_1=4$ and $p_2=1.2$. The validity area for an eventual sensor application is reported in this figure.

minimum of the order of 0.04 (m_{0i}~3) for $\frac{\sigma_{0i}}{\sigma_{max}} \approx 0.5$ (Fig. 11b). Taking these considerations into account, the Eq. (25) is proposed as a general form for the evolution of $\frac{m_{0i}}{m_{max}}$:

$$\frac{m_{0i}}{m_{max}} = \left[1 + \xi_i \frac{\sigma_{0i}}{\sigma_{max}}\left(\frac{\sigma_{0i}}{\sigma_{max}} - 1\right)\right]^{p_i}. \quad (25)$$

If $\frac{m_{0i}}{m_{max}}$ is a minimum for $\frac{\sigma_{0i}}{\sigma_{max}} = 0.5$, then $\xi_i = 4\left[1 - \left(\frac{m_{min}}{m_{max}}\right)^{1/p_i}\right]$, where m_{min} is the minimum value of m_{0i}. Therefore, the relation (25) is rewritten as:

$$\frac{m_{0i}}{m_{max}} = \left[1 - 4\left(1 - \left(\frac{m_{min}}{m_{max}}\right)^{1/p_i}\right)\frac{\sigma_{0i}}{\sigma_{max}}\left(1 - \frac{\sigma_{0i}}{\sigma_{max}}\right)\right]^{p_i} \quad (26)$$

with $m_{min} = 3$, $m_{max} = 78$, and $\sigma_{max} = 5310$ MPa, the p_i exponents have been identified on the experimental values of $\frac{m_{0i}}{m_{max}}$. The two curves drawn in Fig. 11b correspond to Eq. (26) with $p_1 = 4$ and $p_2 = 1.2$.

As a conclusion, the complete identified model (Eq. (27)) for the failure of femtosecond laser beam nano-structured and unstructured fibers is given by Eqs. (12), (24) and (26).

$$P = 1 - \sum_{i=1}^{2} \alpha_i \exp - \left(\frac{\sigma}{\sigma_{0i}}\right)^{m_{0i}} \quad \text{with} \quad \sum_{i=1}^{2} \alpha_i = 1,$$

$$\sigma_{0i} = \sigma_{max}\left[\frac{\beta}{1 + \frac{2\delta_i n_\ell N_\ell}{1 + \frac{3}{n_\ell} I_0\left(\frac{dy}{dy_0}\right)}\left[\mathrm{Ln}\left(\frac{E_p}{E_{p0}}\right)\right]^q} + \frac{1-\beta}{1 + \gamma\left(\mathrm{Ln}\left(\frac{E_p}{E_{p0}}\right)\right)}\right]^r$$

$$m_{0i} = m_{max}\left[1 - 4\left(1 - \left(\frac{m_{min}}{m_{max}}\right)^{1/p_i}\right)\frac{\sigma_{0i}}{\sigma_{max}}\left(1 - \frac{\sigma_{0i}}{\sigma_{max}}\right)\right]^{p_i} \quad (27)$$

$N_\ell = \frac{2\alpha^2 \pi \lambda}{M^2 NA^2 dz}\sqrt{\frac{E_p}{E_{p0}} - 1}$ and $I_0\left(\frac{dy}{dy_0}\right)$ given by the relation (21b).

The parameters of these equations are: $\alpha_1 = 0.55$ ($\alpha_2 = 0.45$), $\beta = 0.74$, $\gamma = 0.69$, $r = 1/4$, $\delta_1 = 0.82$, $\delta_2 = 3.55$, $q = 3.5$, $dy_0 = 2$ μm, $dy_{max} = 22$ μm, $m_{max} = 78$, $m_{min} = 3$, $\sigma_{max} = 5310$ MPa, $p_1 = 4$, and $p_2 = 1.2$ and the optical parameters: a/M = 0.491 [30], $\lambda = 800$ nm, and $NA^2E_{p0} = 15.5$ nJ. To evaluate the pertinence and the possibilities of the model (Eq. (27)) different simulations with $n_\ell = 3$, dx = 5 μm, dy = 7 μm, $1 < E_p/E_{p0} < 3$ and NA = 0.4 (dz = 0.33 μm), 0.8 (dz = 0.25 μm) have been realized. The results, failure probability as a function of the failure stress, have been plotted in Fig. 12. The general tendencies of the experimental failure curves observed in Fig. 7a–b are fairly well restituted and the predictive aspect of this phenomenological model seems demonstrated.

7. Discussions and perspectives

For sensor applications and particularly to use these nano-structured fibers for structural composite monitoring, as an example the detection of maximum strain level in cylindrical composite fuel vessels [5,31,41], for a fixed structuration the range of the failure stresses should be narrow, which involves high values for the Weibull's exponents as those described in the previous model (Eq. (26)). Values of m_{0i} greater than 15 are required ($m_{0i}/m_{max} \geq 0.2$). Taking the strain levels in the composite structure to be detected and the Young's modulus value of the fibers (E~70 GPa) into account, the expected range of the Weibull's stresses is about $500 < \sigma_{0i} < 2000$ MPa, thus $0.1 < \sigma_{0i}/\sigma_{max} < 0.4$. The validity area for sensor application in composite vessels has been reported in the Fig. 11b. The most important parameters to design a conservative sensor are the two scaling parameters σ_{02} and m_{02}. As shown in Fig. 11b, only few points with Weibull's stresses in the range 600 to 1200 MPa are in the sensor validity area ($m_{0i} > 15$). This corresponds to the strain levels of 0.8% to 1.7%, which is about the application domain for pressure composite vessels (0.8% to 2%). However, for $\sigma_{0i} > 1300$ MPa ($\sigma_{0i}/\sigma_{max} > 0.25$) the Weibull's exponents are too low for an eventual sensor application. To overcome this problem a change in the structuration experimental procedure has been tested. Rather than to focus the laser beam in the neighborhood of the surface of the silica, the ΔZ_T translation value has been calculated such that the waist of the beam was located in the core of the fiber, at the vicinity of its center. In that case, according to the work of Juodkazis et al. [42] a confined micro-explosion in the bulk of the silica occurs and nano-void surrounded by densified region appears. The created defects are not superficial craters as in the previous study, but nano-voids in the bulk of the fibers. Three sets of experiments with such focusing condition have been carried out: NA = 0.8, $E_p = 82$ nJ, NA = 0.4, $E_p = 320$ and 800 nJ and the results have been reported in Figs. 7b and 13, respectively. Due to linear and non-linear beam absorption by the silica, for the same pulse energy the failure forces are greater than those obtained with superficial defects (Fig. 13). Hence, for NA = 0.8 and E_p/E_{p0}~3.3 the fracture forces are very close to those of virgin fibers. However, a very interesting and surprising result has been observed for NA = 0.4,

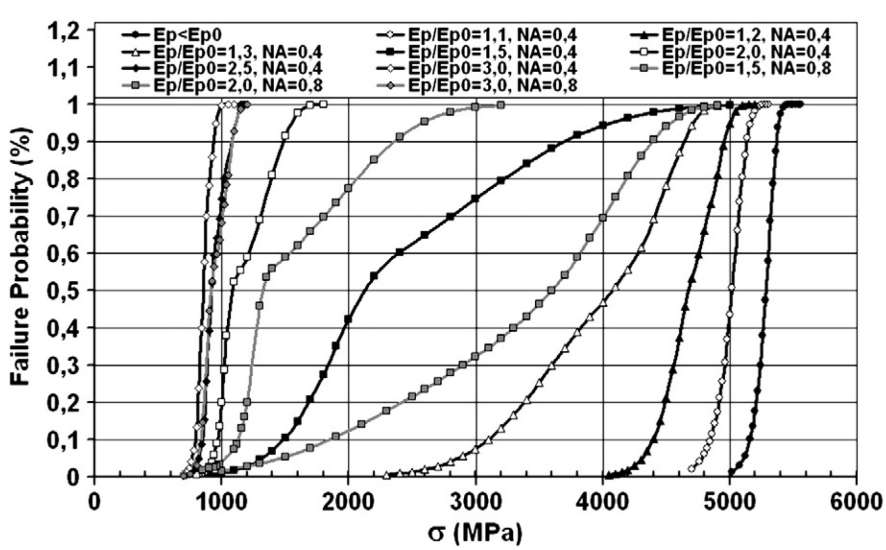

Fig. 12. Some theoretical predictions (Eq. (27)) of the failure probability P for NA = 0.4 and 0.8, and different pulse energy ratios E_p/E_{p0}. The general tendencies of the failure curves are fairly restituted.

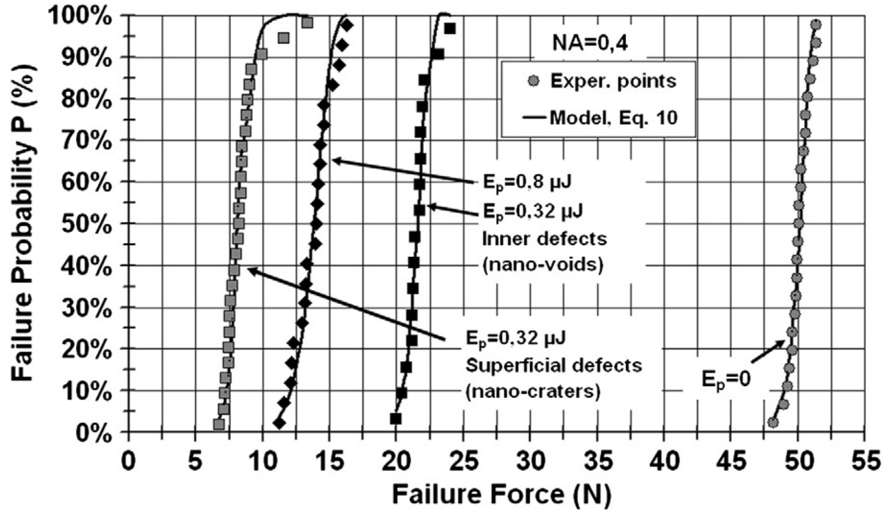

Fig. 13. Comparison for NA = 0.4 and E_p = 320 nJ of the failure probabilities for superficial (nano-craters) and inner (nano-voids) defects. Results for E_p = 800 nJ with inner defects. Experiments and modeling (Eq. (10)). For nano-void structuration the Weibull's parameters (σ_0/σ_{max} = 0.43 and 0.28, m_0/m_{max} = 0.44 and 0.18 for E_p = 320 and 800 nJ, respectively) belong to the sensor validity area reported in Fig. 11b.

E_p = 320 and 800 nJ. As shown in Fig. 13, the range of failure forces is very narrow and the Weibull's parameters (Eq. (10)) identified on the experimental points (continuous lines in Fig. 13) are: $\alpha = 1$, $\sigma_0 =$ 2290 and 1490 MPa, m_0 = 34 and 14 for Ep = 320 and 800 nJ, respectively. Hence, σ_0/σ_{max} = 0.43 and 0.28, m_0/m_{max} = 0.44 and 0.18. These coordinates have been reported in Fig. 11b and the representative point clearly verifies the conditions for sensor applications. This promising result shows that it seems possible to access to a large range of rupture stresses ($0.1<\sigma_0/\sigma_{max}<0.5$) with high Weibull's exponent ($m_0>15$) with adequate nano-structuration procedure. This new kind of fiber structuration is under consideration.

8. Conclusions

Knowing the morphologies and the distribution of nano-craters structured on the surface of optical fibers and generated by near threshold single-shot femtosecond laser the rupture strength of these fibers can be controlled. The value of the ablation threshold energy for optical silica fiber has been determined and is slightly higher than the one reported for borosilicate glass ($NA^2E_{p0(fiber)} = C =$ 15.5 nJ, $NA^2Ep_{0(borosil.)}$ = 11.1 nJ, where NA is the numerical aperture of the objective to focus the laser inside the fibers). An additive combination of two classical Weibull's laws (two Weibull's exponents m_{0i}, two Weibull's scaling stresses σ_{0i} and a balancing parameter α) allows a good representation of the failure probability of the tested fibers (impacted and virgin fibers). For a given fluence ratio $F/F_{oc} = E_p/E_{p0} = E_pNA^2/C$ where F_{0c} is the ablation fluence threshold of the silica fibers, it has experimentally been shown that the Weibull's parameters, particularly the two scaling stresses σ_{0i} depend on the NA for the smallest values of E_p/E_{p0}. The scaling stresses increase with the numerical aperture for a fixed value of E_p/E_{p0}. However, for the highest pulse energy ratios, $E_p/E_{p0}>3$, the Weibull's parameters seem independent of the numerical aperture. A phenomenological model for the evolutions of the Weibull's exponents and Weibull's stresses as a function of the geometries and the distribution of the nano-craters directly linked to the carried nano-structuration procedure have been proposed. Thus the Weibull's parameters depend on the optical properties of the incoming beam (E_p, NA, λ), the z position of the beam waist with respect to the surface of the silica fiber, the interval dx, dy between each crater and the number n_ℓ of created lines. The experimental observed tendencies of the failure probability curves are fairly well described by this model which can be used in the future as a forecast tool.

For an eventual sensor application, to extend the Weibull's scaling stress domain associated to sufficiently high Weibull's exponent ($m_{02}>15$) a new kind of nano-structuration has been proposed. In that case the beam waist is located at the vicinity of the center of the fiber. For the two studied cases with NA = 0.4 the Weibull's exponent values m_0 are in the range 15 to 30. This new promising kind of nano-structuration (nano-voids at the center of the fibers) is under consideration and the results will be presented in a further paper.

Acknowledgments

The authors thank the Conseil Régional de Franche-Comté, France, for funding, P.A. Lacourt, L. Furfaro and F. Courvoisier for the setting of the femtosecond laser.

Appendix A

A.1. Case of unstructured fibers

On the structural level (the fiber), the failure occurs when one flaw within the volume becomes critical; the flaw reaches a critical size a_c. Determining the failure at the structure level is equivalent to finding the "weakest link" of the structure. Now, considering a structure Ω of volume V subjected to any stress field: it can be divided into a large number of elements of volume V_0 (representative volume element subjected to a uniform stress field). In that case, the cumulative failure probability P_F of the structure Ω is related to the cumulative failure probability P_{F0} of a link by [43]:

$$P_F = 1 - \exp\left\{\frac{1}{V_0}\int_\Omega \mathrm{Ln}(1-P_{F0})dV\right\}. \tag{A1}$$

The initial flaws are characterized by an initial flaw distribution density f_0 which depends on their sizes a, their orientation $\underline{n}$ and their geometries ω. Moreover, the critical flaw size a_c is a function of the stress field level characterized by the three principal stresses ($\sigma_1>\sigma_2>\sigma_3$) and the geometrical characteristics $\underline{n}$ and ω of the flaws. Thus P_{Fo} is given by:

$$P_{F0} = \int_{a_c(\sigma_1,\sigma_2,\sigma_3,\underline{n},\omega)}^{\infty} f_0(a,\underline{n},\omega)\,da\; d\underline{n}\; d\omega. \tag{A2}$$

The failure probability P_{F0} of a link is small, $P_{F0} << 1$ and combining (A1) and (A2) the general expression of P_F is recasted as:

$$P_F = 1 - \exp\left[-\frac{1}{V_0}\int_\Omega\left(\int_{a_c(\sigma_1,\sigma_2,\sigma_3,\underline{n},\omega)}^{\infty} f_o(a, \underline{n}, \omega)\,da\ d\underline{n}\ d\omega\right)dV\right]. \tag{A3}$$

In the case of fiber under uniform tension different simplifications have to be done: the flaws are supposed to be described by penny cracks whose geometry is taken into account by a dimensionless factor Y, the tensile stress $\sigma_1 = \sigma$ is uniform through the volume of the fiber and only the cracks loaded under a pure mode I condition are considered. With these hypothesis the critical flaw size $a_c(\sigma_1, \sigma_2, \sigma_3, \underline{n}, \omega)$ is written as:

$$a_c = \left(\frac{K_{1c}}{Y\sigma}\right)^2 \tag{A4}$$

where K_{1c} is the stress intensity factor for the opening mode I. If we assume that the initial flaw size distribution is approximated by a power law function for the large flaw sizes [44]:

$$F_0(a) = \frac{\alpha}{a_0}\left(\frac{a_0}{a}\right)^{p+1}. \tag{A5}$$

Introducing (A4), (A5) into (A3) and integrating this expression leads to the classical Weibull's law (see Eq. (13) in the text):

$$P_F = 1 - \exp-\left(\frac{\sigma}{\sigma_0}\right)^{m_0} \text{ with :}$$
$$m_0 = m_{max} = 2p \text{ and } \sigma_0 = \sigma_{max} = \frac{K_{1c}}{Y\sqrt{a_0}}\left(\frac{V_0}{V}\frac{m}{2\alpha}\right)^{1/m_0}. \tag{A6}$$

Note that the Weibull's scaling stress σ_0 depends on the exponent m_0 (or p) and on the ratio V_0/V. If $m_0 >> 1$ a quasi deterministic failure occurs for $\sigma_0 = K_{1c}/Y\sqrt{a_0}$, relation identical to (A4) with $a_0 = a_c$. For the tested fibers, as $m_{max} \sim 80$ (see Section 5) the relation (A4) can be applied. With $K_{1c} \approx 0.79\ MPa\sqrt{m}$, $Y \sim 1.24$ for penny-shaped cracks and $\sigma_{max} = 5300$ MPa (Section 5) the critical flaw size a_c is equal to 15–16 nm which is a value often reported in the literature ($10 < a_c < 40$ nm).

A.2. Case of structured fibers

A phenomenological framework for the modeling of the failure probability of the structured fibers is proposed in this paragraph. The model must describe the bi-linearity of the failure probability curves (Fig. 7a,b,c), the bi-linearity as a function of the pulse energy of the evolution of the scaling stresses σ_{0i} (Fig. 9a) and the large variability of the m_{oi} exponents ($3 < m_{oi} < 80$). As previously mentioned, two kinds of nano-holes morphologies has been observed, the nano-holes composed of a single crater (Fig. 1a and indexed 1 in the model) or two characteristic craters with very distinct geometries (Fig. 1b and indexed 2 in the model). The rupture always occurs in the structured zone whose volume is noted V_{st}. For each family i of nano-hole morphology the V_{st} volume is supposed to be divided into volume elements V_{0i} subjected to uniform generalized stress field $\underline{\underline{\sigma}}$. So $V_{st} = Ni\ V_{0i}$ where Ni is the number of elements V_{0i} and consequently the probability P_{nF} of un-breaking is given by:

$$P_{nF} = \sum_{i=1}^{2}\alpha_i P_{nF_i} = \sum_{i=1}\alpha_i \prod^{N_i}\left(P_{nF_i}\right)_{V_{0i}}, \sum_{i=1}^{2}\alpha_i = 1. \tag{A7}$$

So, the probability P_F of failure reads as:

$$P_F = 1 - \sum_{i=1}^{2}\alpha_i \exp\left[-\frac{1}{V_{0i}}\int_{\Omega_{st}} \mathrm{Ln}\left(1 - P_{F_{0i}}\right)dV_{st}\right] \tag{A8}$$

where $P_{F0}i$ is the failure probability of the V_{0i} element. This formalism is equivalent to those of the weakest link (Eq. (A1)) but where the equivalent weakest link is composed of two weakest links associated in parallel. Following the same hypothesis as those previously assumed for the unstructured fibers, the general expression of P_F is written as:

$$P_F = 1 - P_{nF}$$
$$= 1 - \sum_i \alpha_i\left[-\frac{1}{V_{oi}}\int_{\Omega_{st}}\left(\int_{a_c\left(\underline{\underline{\sigma}}_i, \underline{n}, \omega\right)}^{\infty} f_{oi}(a, \underline{n}, \omega)\,da\ d\underline{n}\ d\omega\right)dV_{st}\right]. \tag{A9}$$

If the initial flaw size is assumed to be penny-shaped and if the failure initiation occurs in plane perpendicular to the direction of the maximum principal stress, the critical crack size is written as:

$$a_c = \left(\frac{\sqrt{EG_c}}{Y\,\underline{\underline{\sigma}}_i}\right)^2 \tag{A10}$$

where Y is a dimensionless factor, E the Young's modulus, G_c the energy release and $\underline{\underline{\sigma}}_i$ an equivalent uniaxial stress for each flaw family. If $\underline{\underline{\sigma}}_i$ is written as $\underline{\underline{\sigma}}_i = \overline{\sigma}_1 F_i\left(\frac{\sigma_2}{\sigma_1}, \frac{\sigma_3}{\sigma_1}\right)$ where $\overline{\sigma}_1 = \sigma$ is the applied tensile stress, (A10) is rewritten as:

$$a_c = \left(\frac{\sqrt{EG_c}}{Y\overline{\sigma}_1 F_i\left(\frac{\sigma_2}{\sigma_1}, \frac{\sigma_3}{\sigma_1}\right)}\right)^2. \tag{A11}$$

Hence, the critical crack size depends on the stress tri-axiality around the two kinds of nano-holes. Note that for virgin fibers, $F_i\left(\frac{\sigma_2}{\sigma_1}, \frac{\sigma_3}{\sigma_1}\right) = 1$ and $\sqrt{EG_c} = K_{1c}$ (Eq. (A4)). Concerning the initial flaw size distribution of well oriented cracks with respect to the principal stresses (opening in a pure mode I) the exponent of the power law function (A5) is supposed to depend on the tri-axiality function F_i thanks to a g_i function:

$$f_{0i}(a) = \frac{\alpha\ g_i\left(F_i\left(\frac{\sigma_2}{\sigma_1}, \frac{\sigma_3}{\sigma_1}\right)\right)}{a_0}\left(\frac{a_0}{a}\right)^{pg_i\left(F_i\left(\frac{\sigma_2}{\sigma_1}, \frac{\sigma_3}{\sigma_1}\right)\right)+1}. \tag{A12}$$

For unstructured fiber $F_i(0,0) = 1$, $g_i(1) = 1$ and the relation (A12) is identical to (A5). Introducing (A12) into (A9) and integrating the obtained expression taking into account the relation (A10) gives:

$$P_F = 1 - \sum_{i=1}^{2}\alpha_i \exp-\left(\frac{\sigma}{\sigma_{0i}}\right)^{m_{oi}}, \sum_i \alpha_i = 1$$
$$m_{0i} = 2p\,g_i\left(F_i\left(\frac{\sigma_2}{\sigma_1}, \frac{\sigma_3}{\sigma_1}\right)\right) \tag{A13}$$
$$\sigma_{0i} = \frac{\sqrt{EG_c}}{Y\sqrt{a_0}}\frac{1}{F_i\left(\frac{\sigma_2}{\sigma_1}, \frac{\sigma_3}{\sigma_1}\right)}\left(\frac{V_{0i}}{V_{st}}\frac{P}{\beta}\right)^{1/m_{0ii}}.$$

The scaling stresses σ_{0i} and the Weibull's exponent m_{0i} depend on the tri-axiality function F_i. From a phenomenological point of view the advantage of the formulation (A13) compared to those proposed by Maurer et al. [35,36]:

$$P_F = 1 - \exp - \sum_i\left(\frac{\sigma}{\sigma_{0i}}\right)^{m_{0ii}} \tag{A14}$$

is the possibility to describe a very large spectrum of failure probability with very distinct and particular values of σ_{0i}; a plateau for a fixed value of the failure probability can be modeled. A multimodal Duxbury distribution [45] could also describe such behavior but the identification of this model is very complicated. Taking into account the relations (A6) for virgin fibers, the normalized parameters can be written as:

$$\frac{m_{0i}}{m_{max}} = g_i\left(F_i\left(\frac{\sigma_2}{\sigma_1},\frac{\sigma_3}{\sigma_1}\right)\right)$$
$$\frac{\sigma_{0i}}{\sigma_{max}} = \left(\frac{V_{0i}}{V_{st}}\frac{P}{\alpha}\right)^{\frac{1}{m_{oi}}}\left(\frac{V}{V_0}\frac{\alpha}{P}\right)^{\frac{1}{m_{max}}}\frac{\sqrt{EG_c}}{K_{1c}}\frac{1}{F_i\left(\frac{\sigma_2}{\sigma_1},\frac{\sigma_3}{\sigma_1}\right)}. \tag{A15}$$

As the V_{0i}/V_{st} ratio is small, as $m_{max} >> 1$, as $m_{0i} > 3$, as $\sqrt{EG_c} \approx K_{1c}$ and finally as the only considered mode along each principal direction is the mode I, the relations (A15) are simplified:

$$\frac{m_{0i}}{m_{max}} = g_i\left(\frac{\sigma_{0i}}{\sigma_{max}}\right) \text{ and } \frac{\sigma_{0i}}{\sigma_{max}} = \frac{1}{F_i\left(\frac{\sigma_2}{\sigma_1},\frac{\sigma_3}{\sigma_1}\right)}. \tag{A16}$$

The tri-axiality function F_i must be evaluated at two different scales j; the scale of the homogenized global nano-structuration (j = 1) and the scale of an individual nano-hole (j = 2). Thus, as these scales are simultaneously present the F_i function is postulated as:

$$\frac{1}{F_i\left(\frac{\sigma_2}{\sigma_1},\frac{\sigma_3}{\sigma_1}\right)} = \frac{\beta}{F_{i1}\left(\frac{\sigma_2}{\sigma_1},\frac{\sigma_3}{\sigma_1}\right)} + \frac{1-\beta}{F_{i2}\left(\frac{\sigma_2}{\sigma_1},\frac{\sigma_3}{\sigma_1}\right)}$$
$$= \sum_{j=1}^{2}\frac{\beta_j}{F_{ij}\left(\frac{\sigma_2}{\sigma_1},\frac{\sigma_3}{\sigma_1}\right)} \text{ with } \sum_j \beta_j = 1 \tag{A17}$$

So, as $F_{ij}(0,0) = 1$, $\sigma_{0i}/\sigma_{max} = 1$ for unstructured fibers.

If the equivalent rupture stress $\overline{\overline{\sigma}}_i$ is defined from the ratio of energy release, the F_i function is equal to:

$$F_i = 1 + \sqrt{\frac{\sigma_n^2 + \tau_n^2}{\sigma_1^2}} \tag{A18}$$

where σ_n and τ_n are the normal and the tangential stresses, respectively. For each considered principal direction (2 and 3), the stress concentration factor is defined by: $K_{T2} = 1 + \frac{\sigma_2}{\sigma_1}$ *and* $K_{T3} = 1 + \frac{\sigma_3}{\sigma_1}$ and the application of the relation (A18) for the mode I gives:

$$F_i = 1 + \frac{\sigma_2}{\sigma_1} = K_{T_2} \text{ and } F_i = 1 + \frac{\sigma_3}{\sigma_1} = K_{T_3} \tag{A19}$$

for the 2 and 3 directions, respectively.

A new value $K_{T_{eq}}$ of the stress concentration factor over the stress field generated by the structuration is written as:

$$K_{T_{eq}} \approx \sqrt{\frac{K_{T_2}^2 + K_{T_3}^2}{2}} \approx \frac{K_{T_2} + K_{T_3}}{2} \approx 1 + \frac{\sigma_2 + \sigma_3}{2\sigma_1}. \tag{A20}$$

The two stress ratios $\frac{\sigma_2}{\sigma_1}$ and $\frac{\sigma_3}{\sigma_1}$ intimately depend on the geometry of the nano-craters and on the parameters of the structuration, thus the tri-axiality function can be rewritten as:

$$F_i = 1 + f_i^*(nano{-}struct.). \tag{A21}$$

where f_i^* is a function depending on the parameters of the structuration. Finally the relation (A17) reads as:

$$\frac{1}{F_i\left(\frac{\sigma_2}{\sigma_1},\frac{\sigma_3}{\sigma_1}\right)} = \sum_{j=1}^{2}\frac{\beta_j}{1 + f_{ij}^*(nano{-}struct)} \text{ with} \sum_j \beta_j = 1. \tag{A22}$$

The Eqs. (A16) and (A22) constitute the foundation of the model and the two functions $g_i\left(\frac{m_{0i}}{m_{max}}\right)$ and $f_{ij}^*(nano{-}struct.)$ will be identified in the Section 6 of the text.

References

[1] N.D.W. Glossop, S. Dubois, W. Tsaw, M. Leblanc, J.L. Lymer, R.M. Measures, R.C. Tennyson, Optical fibre damage detection for an aircraft composite leading edge, Composites 21 (1990) 71–80.
[2] D. Inaudi, A. Elamari, L. Pflug, N. Gisin, J. Breguet, S. Vurpillot, Low-coherence deformation sensors for the monitoring of civil-engineering structures, Sensors Actuators A44 (1994) 125–130.
[3] M.C. Hastings, B. Chiu, D.W. Nippa, Engineering development of optical fiber sensors for adverse environments, Nucl. Eng. Des. 167 (1997) 239–249.
[4] T.S. Jang, J.J. Lee, D.C. Lee, The mechanical behavior of optical fiber sensor embedded within the composite laminate, J. Mater. Sci. Lett. 34 (1999) 5853–5860.
[5] B. Glisic, D. Inaudi, Health monitoring of a full composite tanks using long-gage fiber optic sensors, 11th SPIE's Annual International Symposium on Smart Structures and Materials, 2004, p. 5384.
[6] L. Sorensen, T. Gmürt, J. Botsis, Residual strain development in an AS4/PPS thermoplastic composite measured using fibre Bragg grating sensors, Compos. A 37 (2005) 270–281.
[7] V. Lanticq, M. Quiertant, E. Merliot, S. Delepine-Lesoille, Brilloin sensing cable design and experimental validation, IEEE Sensors J. 8 (7) (2008) 1194–1201.
[8] C.R. Kurkjian, U.C. Peak, Single-valued strength of perfect silica fibers, Appl. Phys. Lett. 42 (1983) 251–253.
[9] C.R. Kurkjian, J.T. Krause, M.J. Matthewson, Strength and fatigue of silica optical fibers, J. Lightwave Technol. 9 (7) (1989) 1360–1370.
[10] J. Matthewson, Optical fiber mechanical testing techniques, Crit. Rev. Opt. Sci. Technol. CR50 (1993).
[11] C.P. Chen, T.H. Chang, Fracture mechanics evaluation of optical fibers, Mater. Chem. Phys. 77 (2002) 110–116.
[12] N. Gougeon, R. El Abdi, M. Poulain, Mechanical reliability of silica optical fibers, J. Non-Cryst. Solids 316 (2003) 125–130.
[13] S. Bhaumik, Effect of humidity of drawing environment on dynamic fatigue of polymer coated high strength silica optical fibers wire, Int. J. 38 (3) (2005) 194–198.
[14] I. Severin, R. El Abdi, M. Poulain, Strength measurements of silica optical fibers under severe environment, Opt. Laser Technol. 39 (2007) 435–441.
[15] R. El Abdi, A. Pujinsky, C. Borda, I. Severin, M. Poulain, New method for strength improvement of silica optical fibers, Opt. Lasers Eng. 36 (2008) 222–229.
[16] S.L. Semjonov, C.R. Kurkjian, Strength of silica optical fibers with micro size flaws, J. Non-Cryst. Solids 283 (2001) 220–224.
[17] R.R. Gattass, E. Mazur, Femtosecond laser micromachining in transparent materials, Nat. Photonics 2 (4) (2008) 219–225.
[18] W. Yang, P.G. Kazansky, Y.P. Svirbo, Non-reciprocal ultrafast laser writing, Nat. Photonics 2 (2) (2008) 99–104.
[19] P.P. Pronko, S.K. Dutta, J. Squier, J.V. Rudd, D. Du, G. Mourou, Machining of submicron holes using a femtosecond laser at 800 nm, Opt. Commun. 114 (1–2) (1994) 106–110.
[20] M. Lenzner, J. Kruger, S. Sartania, Z. Cheng, C. Spielmann, G. Marron, et al., Femtosecond optical breakdown in dielectrics, Phys. Rev. Lett. 80 (18) (1998) 4076–4079.
[21] A. Chimmalgi, T.Y. Choi, C.P. Grigoropoulos, C.P. Komvopoulos, Femtosecond laser aperturless near-field nanomachining of metals assisted by scanning probe microscopy, Appl. Phys. Lett. 82 (8) (2003) 1146–1149.
[22] A.P. Joglekar, H. Liu, G.J. Spooner, E. Meyhofer, G. Mourou, A.J. Hunt, A study of the deterministic character of optical damage by femtosecond laser pulses and application to nanomachining, Appl. Phys. B Lasers Opt. 77 (1) (2003) 25–30.
[23] S.S. Mao, F. Quere, S. Guizard, X. Mao, R.E. Russo, G. Petite, et al., Dynamics of femtosecond laser interactions with dielectrics, Appl. Phys. A: Mater. Sci. Process. 79 (7) (2004) 1695–1709.
[24] J. Koch, F. Korte, C. Fallnich, A. Ostendorf, B.N. Chichbou, Direct-write subwave length structuring with femtosecond laser pulses, Opt. Eng. 44 (5) (2005) 051103.
[25] E.G. Gamaly, A.V. Rode, B. Luther-Davies, V.T. Tikhonchuk, Ablation of solids by femtosecond lasers: ablation mechanism and ablation threshold for metals and dielectrics, Phys. Plasmas 9 (3) (2002) 949–957.
[26] T.Q. Jia, Z.Z. Xu, X.X. Li, X. Li, B. Shuai, F.L. Zhao, Microscopic mechanisms of ablation and micromachining of dielectrics by using femtosecond lasers, Appl. Phys. Lett. 82 (24) (2003) 4382–4384.
[27] D. Bouilly, D. Perez, L.J. Lewis, Damage in materials following ablation by ultra-short laser pulses. A molecular dynamics study, Phys. Rev. B 76 (2007) 184119.
[28] P. Polesana, M. Franco, A. Couairon, D. Faccio, P. Di Trapani, Filamentation in Kerr media from pulsed Bessel beam, Phys. Rev. A 77 (2008) 043814.
[29] B. Delobelle, F. Courvoisier, P. Delobelle, Morphology study of femtosecond laser nano-structured borosilicate glass using atomic force microscopy and scanning electron microscopy, Opt. Lasers Eng. 48 (2010) 616–625.
[30] B. Delobelle, R. Salut, F. Courvoisier, P. Delobelle, A detailed study through the focal region of near-threshold single-shot femtosecond laser ablation nano-holes in borosilicate glass, Opt. Commun. 284 (2011) 5746–5757.
[31] Delobelle B., Développement d'une nouvelle génération de capteur à fibre optique pour le suivi de l'intégrité d'un réservoir de stockage d'hydrogène sous haute pression, Thesis FEMTO-ST Institute, Depart. of Applied Mech., Univ. of Besançon, France, 2009.
[32] S. Xu, J. Qju, T. Jia, H. Sun, Z. Xu, Femtosecond laser ablation of crystals SiO_2 and YAG, Opt. Commun. 274 (2007) 163–166.
[33] W. Weibull, A statistic theory of the strength of materials, Ing. Vetenskaps Akademien, Handlingar 151 (3) (1939) 45–55.
[34] W. Weibull, A statistic distribution function of wide applicability, J. Appl. Mech. 18 (1951) 293–297.
[35] R.D. Maurer, Strength of fiber optical waveguides, Appl. Phys. Lett. 27 (4) (1975) 220–221.

[36] R. Olshansky, R.D. Maurer, Tensile strength and fatigue of optical fibers, J. Appl. Phys. 47 (10) (1976) 4497–4499.
[37] C.R. Kurkjian, R.V. Albarino, J.T. Krause, H.N. Vazirani, F.U. Di Marcello, S. Torza, H. Schonhorn, Strength of 0.04–50 m lengths of coated fused silica fibers, Appl. Phys. Lett. 28 (10) (1976) 588–590.
[38] J.E. Ritter, J.M. Sullivan, K. Jakus, Application of fracture mechanics theory to fatigue failure of optical glass fibers, J. Appl. Phys. 49 (9) (1978) 4779–4782.
[39] C.E. Inglis, Stresses in a plate to the presence of cracks and sharp corner, Trans. Int. Archit. 55 (1913) 219–230.
[40] L. Afferrante, M. Ciavarella, E. Valenza, Is Weibull's modulus really a material constant ? Example case with interacting collinear cracks, Int. J. Solids Struct. 43 (2006) 5147–5157.
[41] N. Takeichi, H. Senoh, T. Yokota, H. Tsuruta, K. Hamada, H.T. Takeshita, H. Tanaka, T. Kiyobayashi, T. Takano, N. Kuriyama, Hybrid hydrogen storage vessel, a novel high pressure hydrogen storage vessel combined with hydrogen storage material, Int. J. Hydrog. Energy 28 (2003) 1121–1129.
[42] S. Juodkazis, H. Misawa, T. Hashimoto, E. Gamaly, B. Lutha-Davies, Laser-induced microexplosion confined in a bulk of silica: formation of nano-voids, Appl. Phys. Lett. 88 (2006) 201905.
[43] A.M. Freudenthal, Statistical approach to brittle fracture, in: H. Liebowitz (Ed.), Fracture, 2, Academic Press, 1968, pp. 591–619.
[44] A.D. Jayatilaka, K. Trustrum, Statistical approach in brittle fracture, J. Mater. Sci. 2 (1977) 1426–1430.
[45] A. Duxbury, Breakdown of diluted and hierarchical systems, in: Herman, Roux (Eds.), Statistical Models for the Fracture of Disordered Media, Elsevier Science Publishers, 1990, pp. 183–228.